Terahertz conductivity of two-dimensional materials: a review

Shuva Mitra

E-mail: smitra8@wisc.edu

Laleh Avazpour

E-mail: laleh.avazpour@wisc.edu

Irena Knezevic

E-mail: irena.knezevic@wisc.edu
Department of Electrical and Computer Engineering, University of Wisconsin-Madison, 1415 Engineering Dr., Madison, WI 53706, USA

Abstract. Two-dimensional (2D) van der Waals materials are shaping the landscape of next-generation devices, offering significant technological value thanks to their unique, tunable, and layer-dependent electronic and optoelectronic properties. Time-domain spectroscopic techniques at terahertz (THz) frequencies offer noninvasive, contact-free methods for characterizing the dynamics of carriers in 2D materials. They also pave the path toward the applications of 2D materials in detection, imaging, manufacturing, and communication within the increasingly important THz frequency range. In this paper, we overview the synthesis of 2D materials and the prominent THz spectroscopy techniques: THz time-domain spectroscopy (THz-TDS), optical-pump THz-probe (OPTP) technique, and optical pump–probe (OPP) THz spectroscopy. Through a confluence of experimental findings, numerical simulation, and theoretical analysis, we present the current understanding of the rich ultrafast physics of technologically significant 2D materials: graphene, transition metal dichalcogenides, MXenes, perovskites, topological 2D materials, and 2D heterostructures. Finally, we offer a perspective on the role of THz characterization in guiding future research and in the quest for ideal 2D materials for new applications.

1. Introduction

Since the discovery of graphene [1], a variety of two-dimensional (2D) materials have emerged, unveiling both rich new physics that stems from reduced dimensionality and opening doors to exciting new applications and next-generation devices. 2D materials are room-temperature-stable layered structures with strong intralayer covalent bonds and weak interlayer van der Waals (vdW) bonds [2]. To date, over five thousand compounds and layered structures have been identified, with more than five hundred 2D materials already synthesized in laboratories [3]. Noteworthy examples of this new class of materials include transition metal dichalcogenides (TMDs), transition metal carbides/carbon nitrides (MXenes), 2D perovskites, phosphorene, silicene, germanene, and 2D oxides. The bandgaps of 2D materials range from zero for graphene [1], to a few meV for silicene and germanene [4], to a few eVs for TMDs, and over 5 eV for oxides [5]. 2D materials find applications in transistors [6], phototransistors [7, 8], photodetectors [9], light-emitting diodes [10], and solar cells [11].

Beyond the high carrier mobility, 2D materials exhibit interesting spin-valley physics induced by robust spin-orbit coupling. Owing to the reduced dimensionality and the resulting reduced dielectric screening, Coulomb interactions in 2D materials play an important role in electronic transport [12]. In TMDs, limited screening results in the formation of excitons and trions with binding energies that reach hundreds of meV [13, 14, 15]. The prevalence of excitonic and trionic emission at room temperature is a consequence of these high binding energies. The many-body physics of excitons and trions, alongside single-particle electronc transport governed by electron interactions with phonons, impurities, boundaries, and defects, results in interesting electronic and optoelectronic responses, revealed particularly well via ultrafast experiments on femtosecond-to-picosecond timescales [16].

The terahertz (THz) part of the electromagnetic spectrum, with frequencies ranging from 0.1 THz to 10 THz (see Fig. 1(a)), fills the gap between the microwave and the infrared, offering nonionizing radiation suitable for noninvasive detection and probing. This frequency band is important for fundamental materials exploration, given that the scattering rates of charge carriers, materials vibrational excitations, and many-body correlated phenomena in both bulk semiconductors and 2D materials fall within this range (see Fig. 1(b)). Terahertz devices [19] are a bridge between lower-frequency electronic and higher-frequency photonic devices, and their applications span imaging [20, 21, 22], communication [23, 24, 25, 26], and manufacturing [27, 28, 29]. Selection of materials for next-generation ultrafast 6G communication technology, which will operate at 200 GHz and beyond (this includes core technology devices such as antennas, modulators, and detectors, as well as edge devices [30, 31, 32]) requires detailed information about THz materials conductivity. In addition, THz field-effect transistors are in development and being introduced into integrated circuits [33, 34, 35, 36], and conductivity is a key parameter for determining their channel performance. In manufacturing, quality control in sensing and imaging applications requires materials with high yet fairly frequency-independent conductivity, which certain 2D materials such as MXenes possess. Figure 1(c) shows various applications in different parts of the THz frequency band. Unsurprisingly, the key to unlocking the potential of 2D materials for myriad applications lies in their comprehensive experimental characterization, aided by detailed microscopic theory.

THz spectroscopies provide contact-free, nondestructive, and noninvasive characterization of near-equilibrium and nonequilibrium carrier dynamics in materials

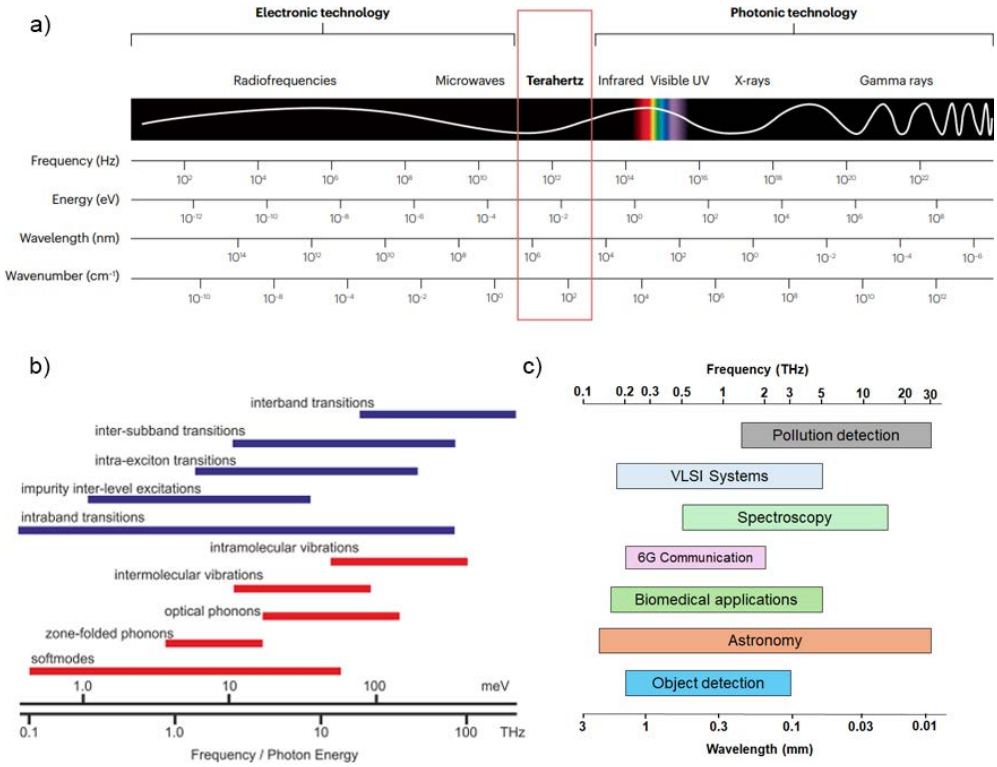

Figure 1. (a) The electromagnetic spectrum, where the THz band resides between the typical electronic-application band to the left and the photonic-application band to the right. Reprinted with permission from [17], Copyright 2023, Nature Publishing Group. (b) The electronic and phononic excitations occurring in the THz band. Blue shows electronic and red shows phononic excitations. Reprinted with permission from [18]. Copyright 2019, IOP Publishing. (c) Representation of different applications in the terahertz spectrum.

at THz frequencies [37, 38], in contrast to traditional electronic transport measurements, which are prone to uncertainties due to contact resistance, Schottky-barrier formation, and sample damage [39]. THz spectroscopy techniques offer direct access to time- and frequency-resolved conductivity, a quantity that provides insights into the behavior of charge carriers, exciton and trion binding energies, interband and intraband electron transitions, surface-electron dynamics, as well as phonon and plasmon resonances [40, 41, 42, 12, 43]. Widely used time-resolved techniques are THz time-domain spectroscopy (THz-TDS), optical pump terahertz probe spectroscopy (OPTP), and optical pump–probe (OPP) THz spectroscopy. THz-TDS probes equilibrium carrier dynamics, providing real and imaginary parts of the conductivity without relying on Kramers-Kronig relations. OPTP extracts photoconductivity, offering insights into the relaxation dynamics of photoexcited carriers, which includes both radiative and nonradiative recombination processes, and the formation and recombination of excitons and trions [44, 45]. OPP combines elements of ultrafast laser spectroscopy and THz spectroscopy to study the dynamics of photoexcited carriers [46, 47, 48].

This article presents a comprehensive review of recent progress in experimental

and theoretical efforts to understand THz conductivity and photoconductivity in 2D vdW materials. Section 2 discusses the synthesis process of 2D materials, while Sec. 3 provides a brief overview of time-domain THz spectroscopic techniques. Section 4 explores phenomenological, numerical, and quantum-mechanical models of conductivity. Section 5 reviews experimental and numerical findings on the THz response of 2D materials, specifically graphene, TMDs, MXenes, perovskites, topological 2D materials, and heterostructures. Finally, Sec. 6 concludes with remarks and future outlook.

2. Synthesis of 2D Materials

In this section, we delve into the techniques used for synthesizing graphenelike materials such as h-BN, TMDs, graphitic carbon nitride (g-C_3N_4), black phosphorous (BP), silicene, and MXenes. Three general approaches—micromechanical, ion-intercalation, and liquid phase—have been developed to break the weak van der Waals attraction between adjacent layers of TMDs or graphene and form few-layer films or monolayers of these materials from a bulk sample. These methods can be grouped into two large categories: "bottom up" and "top down."

In bottom-up approaches, individual constituents are systematically assembled to form more complex structures. Conversely, top-down techniques involve the disassembly or breakdown of a layered precursor material. In the case of graphene, this typically involves starting with natural crystals like graphite or artificially synthesized materials, such as highly oriented pyrolytic graphite, monolayers, or a few-layers flakes, and then reducing or thinning them to achieve the desired graphenelike structures. Various exfoliation techniques are among top-down methods.

2.1. Chemical vapor deposition

Chemical vapor deposition (CVD) stands as a prominent precision-driven technique in the synthesis of 2D materials, including TMDs and graphene. This method showcases the immense potential for breakthroughs in materials science, as supported by various studies [49, 50, 51, 52]. In the CVD process, a gaseous precursor containing the constituent atoms or molecules of the desired material is introduced into a high-temperature reactor chamber. Within this chamber, the precursor undergoes chemical reactions and deposits as a thin film on a substrate.

CVD enables exceptional control over key properties of the resulting 2D materials, such as layer thickness, crystallinity, and composition. This precision makes CVD indispensable for a wide range of applications in nanoelectronics, photonics, and beyond, as evidenced by various studies [53, 54, 55].

One noteworthy development in CVD techniques is the introduction of a capping technique by Tsigkourakos for chemical vapor deposition of large and uniform MoS_2 flakes [56]. Figure 2(a) shows the typical growth process of TMD layers via CVD. This innovation has expanded the possibilities for MoS_2 synthesis. Additionally, CVD has been instrumental in successfully growing monolayer MoS_2 on a large scale, as demonstrated in the study by Pelella *et al.* [57]. The precision of CVD is highlighted by its ability to control the properties of the resulting samples and minimize contamination [58, 59].

Metal-organic chemical vapor deposition (MOCVD), which has been traditionally used to deposit III–V and II–VI compounds, is appealing because of the higher purity

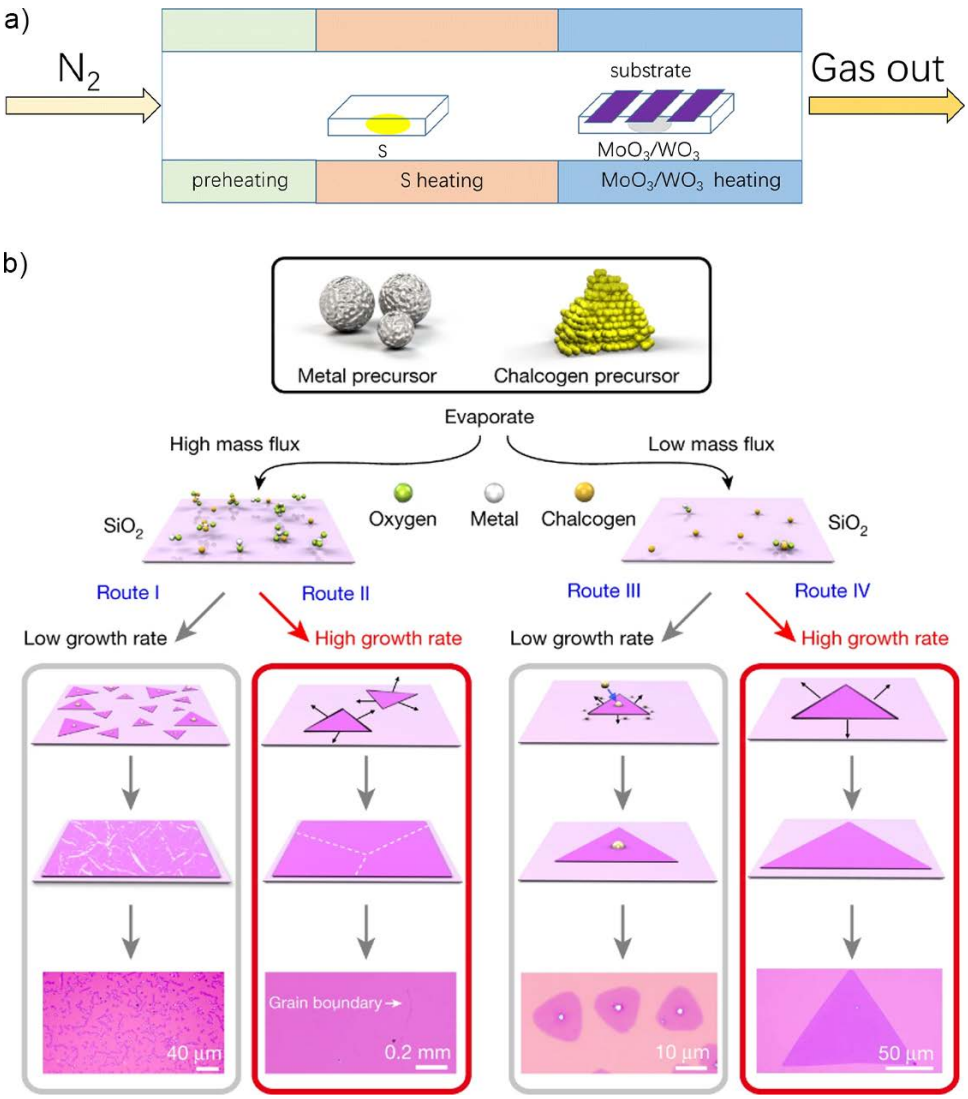

Figure 2. (a) Schematic of a typical CVD growth process for 2D TMDs. Reprinted with permission from [64]. Copyright 2020, Springer-Nature. (b) Dependence of TMD sample characteristics on mass flux and growth rate. High metal precursor flux makes samples polycrystalline whereas low flux makes them single-crystalline. High growth rate results in large grain sizes, or, in the case of single-crystal growth, large TMD samples. Reprinted with permission from [65]. Copyright 2018, Nature Publishing Group.

organometallic compounds used in deposition of 2D semiconducting 2H–TMDS, as required in optoelectronic and high-performance electronic applications [60, 61, 62]. MOCVD can grow large-scale, uniform samples [63].

The exfoliation of graphite techniques limit sample size to small flakes, which are not useful in THz studies, where long wavelengths require large-area samples. As a result, CVD, specifically MOCVD is commonly used because of its advantage of

growing large-size samples at a faster rate. For example, in experiments performed by Ruan *et al.* [66], single-layer graphene was grown from a solid-state carbon source on copper foil with PMMA present at 800-1000°C [67]. Low-pressure H_2/Ar gas mixture was introduced and subsequently transferred onto SiO_2 substrate. A similar technique was followed to prepare single and few-layer graphene in [68, 69, 70]. Monolayer MoS_2 grown directly on sapphire was obtained from precursor MoO_3 reacting with sulfur powder at 650 °C and 10 Torr pressure [71] for 10 minutes. Trilayer MoS_2 was grown in a two-step thermolysis process with $(NH_4)_2MoS_4$ baked at 120°C for 30 min. Yan *et al.* [72] grew few-layer WS_2 samples on sapphire using WO_3 as a precursor for tungsten at 1000 °C for 30 minutes. Depending on the flux rate of metal precursor and growth rate, samples can be grown with varying crystallinity and grain size as shown in Fig. 2(b). Although CVD growth of MXenes and perovskites faced difficulties in the past, recent technological improvement has made it possible to grow them. Wang *et al.* [73] recently demonstrated the growth of MXenes by CVD, where they used CH_4 and $TiCl_4$ gas mixture at 950 °C on Ti surface. Sn-Pb based 2D perovskite thin films were recently grown after $SnCl_2$/$PbCl_2$ precursor in a phenylethylamine iodide (PEAI) atmosphere that underwent transformation at 100 °C [74]. To our knowledge, CVD-grown MXenes and perovskites are yet to be tested using THz spectroscopic techniques.

2.2. Molecular beam epitaxy

Molecular beam epitaxy (MBE) is a sophisticated physical vapor deposition technique designed for the epitaxial growth of single-crystalline thin films. Epitaxial growth involves the incremental deposition of thin film layers atop a crystalline substrate, which results in good alignment of the crystal structure between the film and the substrate. Within this process, atoms or molecules individually adhere to the substrate's surface, which produces thin films with atomic-level composition control.

MBE growth unfolds within the confines of a vacuum chamber, where one or more thermal energy beams of atoms or molecules are directed onto a substrate. As the atoms or molecules condense on the substrate, a thin film is grown [75]. The incorporation of exceptionally pure source materials (typically 99.9999%) and the establishment of an ultra-high-vacuum growth environment (typically maintained at pressures lower than 10^{-9} Torr) helps prevent contamination within the material. Moreover, the lower growth temperatures inherent to MBE facilitate the creation of vertical heterostructures with minimal degradation or intermixing/interaction among distinct materials.

In all, MBE has several advantages over other thin-film deposition techniques, such as sputtering or CVD. First, MBE offers a high degree of control over the film growth process, including the film thickness, composition, and doping level. Second, MBE can be used to grow high-quality, single-crystal films with sharp interfaces. Third, MBE is a versatile technique that can be used to grow a wide variety of materials, including semiconductors, metals, oxides, and nitrides. [76].

Thanks to the inherent advantage of precision without sacrificing growth rate, MBE has been the primary growth method for topological insulators (TI) such as Bi_2Se_3, Bi_2Te_3, and Sb_2Te_3, which require careful maintenance of stacking order (for example, Se–Bi–Se–Bi–Se in Bi_2Se_3 known as a quintuple layer (QL) along the c-axis direction [77, 78]). Typically, a two-step growth method is followed to grow TIs: a low-temperature nucleation layer is grown to compensate for dangling bonds,

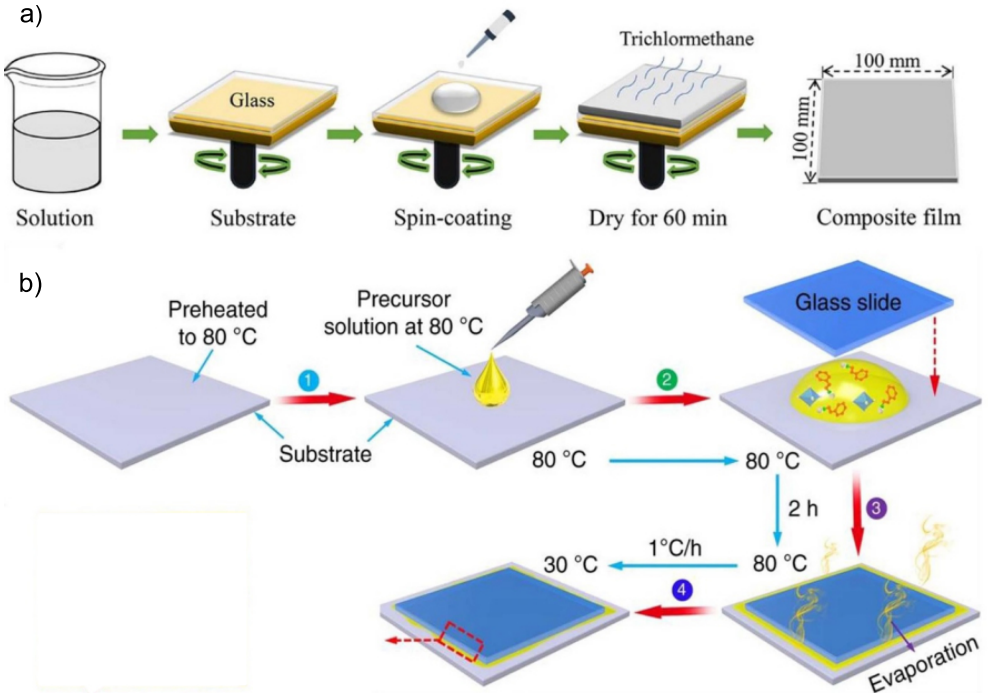

Figure 3. Fabrication process for 2D perovskites. (a) Spin-coating method, where a precursor-carrying solvent is gradually poured onto a spinning substrate. Trichloromethane/PMMA is deposited, followed by drying for grain size reduction. Adapted with permission from [88]. Copyright 2020, American Chemical Society. (b) Induced peripheral crystallization (IPC) method, where a hot precursor solution is dripped on then sandwiched between substrate and a glass slide on top. At high temperatures, nucleation occurs at the edge of the top glass slide. Adapted with permission from [89], CC–BY 4.0.

followed by annealing and deposition of the thin films [79]. Bi_2Se_3 on sapphire or silicon substrates were grown where van der Waals epitaxy compensates 15% lattice mismatch. Typical Knudsen-type cells supply Se flux. However due to the outgassing of Se from the substrate, Se:Bi pressure is kept at 15:1 to 20:1 [80, 81, 82]. Bansal *et al.* [81] grew Bi_2Se_3 on undoped Si substrates in high vacuumm pressure 9×10^{-8} Pa at 860 °C substrate temperature and later the thin films grown were characterized using THz-TDS and OPTOP measurements [83]. The growth rate for Bi_2Se_3 is usually around 1 QL/min [84]. While Bi_2Te_3 follows a similar growth method, $Sb2_2Te_3$ growth parameters are being actively researched, with growth rates ranging 0.2-2 QL/min, substrate temperatures 200-320 °C, Te:SB flux ratios from 2:1 to 20:1 [85, 86, 87].

2.3. Spin-coating technique

Compared to traditional 2D materials, 2D perovskites are more complicated to grow over a large area using vapor deposition techniques. The general recipe for synthesizing 2D perovskites involves introducing them in liquid phase to a substrate via spin-coating techniques. The key challenge lies in improving the wettability of the polar perovskite polymer with polar solutions, which is required for the polymer to adhere

to polar substrates such as glass [90]. Introducing intermediate polar solvents, such as dimethyl sulfoxide (DMSO) or γ-butyrolactone (GBL), is used to make the solvent polar. Burgos-Caminal *et al.* [91] used an antisolvent method, in which precursor solutions—BuAI or PEAI (1 mmol)and PbI_2 (0.5 mmol)—was dissolved in 1 mL of DMSO and spun for 10 s at 1000 rpm, followed by 6000 rpm for 30 s, and annealed at 100 °C . Chlorobenzene acted as an antisolvent to facilitate the crystallization process. The sample was then measured by TRTS process. Cao *et al.* [88] were able to grow polycrystalline $(PEA)_2SnBr_4$ perovskite thin films via the spin-coating method. The 2D perovskite was treated with ice-water and dissolved in PMMA/trichloromethane solution as shown in Fig. 3(a) to reduce grain size. After drying, they were able to achieve 100 μm thick film with 100 mm $\times$ 100 mm size area. Liu *et al.* [89] introduced the induced peripheral crystallization (IPC) technique, where temperature-controlled crystallization preferentially happened in the glass edge with a small lateral area on the top surface. The IPC process is shown in Fig. 3(b). The area of the sample was reported over 2500 mm^2, well suited for THz experiments. Growth of single-crystalline 2D perovskites, monolayer or few-layer, has not been reported.

2.4. Exfoliation techniques

For completeness, in this section we present an overview of exfoliation techniques, but note that it is difficult to produce large-area samples required for THz experiments using exfoliation.

Mechanical exfoliation involves precise cleavage of layered materials, such as graphite or bulk TMD crystals, into atomically thin two-dimensional sheets. This is accomplished through the application of mechanical force, typically using adhesive tape. Novoselov *et al.* [92] successfully synthesized graphene from graphite using the Scotch-tape method in 2004. These tapes are typically made from well-known polymers like polymethylmethacrylate (PMMA) [93]. The resulting monolayer or few-layer sheets exhibit extraordinary electronic, optical, and mechanical properties, which makes them ideal candidates for next-generation electronic devices, sensors, and energy storage systems. For example, they can serve as the channel material for fabricating interband tunnel field-effect transistors (FETs) that exhibit lower power consumption than classical transistors [94, 95].

To transfer the thin film from the tape to a target substrate, scientists typically press the tape onto the substrate, such as a silicon wafer or another suitable material. Gentle pressure, solvent, and sometimes heat are applied to ensure good adhesion between the thin film and the substrate [96]. However, completely removing the tape can be quite challenging. Thermal treatment, for instance, may introduce defects and oxidized p-type doping to the materials [97]. On the other hand, acetone and other solvents used for rinsing often leave chemical and organic residues on the resulting nanolayer after the transfer, and this rinsing process can be time-consuming and environmentally unfriendly [98]. Depending on the material and intended application, additional steps like annealing or chemical processing may be necessary to improve the quality and properties of the transferred thin film.

Mechanical exfoliation has limitations in terms of yield for high-quality monolayers. While it provides sufficient material for laboratory experiments, scaling up production can be challenging [99, 92]. Nevertheless, recent years have seen the introduction of improved mechanical exfoliation techniques designed to facilitate scale-up, such as the spin pumping automated mechanical exfoliation technique [100].

Liquid exfoliation involves dispersing bulk TMD crystals or graphite flakes into a liquid solvent, followed by direct exfoliation aided by shear force or ultrasound-induced acoustic cavitation [101, 102, 103, 104]. This technique utilizes organic solvents, water/surfactant systems, or ionic liquids as a medium to disperse bulk samples and extract nanolayers. Liquid exfoliation offers several advantages, including scalability, cost-effectiveness, and the ability to produce large quantities of high-quality two-dimensional materials.

The resulting suspension contains atomically thin layers of the desired material, which can be readily deposited onto various substrates by submerging the substrate in the emulsion. This approach allows precise control over thickness and properties. Several factors, including the power of ultrasound, shear rate, concentration of bulk material [105], and solvent and surfactant properties [106, 107], influence the quality of the resulting layers [108, 109]. Researchers have explored various techniques, such as salt-assisted refluxing and ethylenediamine-assisted exfoliation, to effectively exfoliate materials like MoS_2 nanosheets and obtain high-yield monolayer extraction [110, 111]. Novel methods, like hydrazine-assisted ball milling, have also been introduced to fabricate high-quality TMD nanoflakes through a combination of chemical intercalation and mechanical exfoliation [103]. The same process can be performed using shock waves for ablation of TMD materials [112].

While chemical exfoliation, particularly via ion intercalation, is commonly used for bulk materials, it can sometimes alter the quality of the resulting 2D material. For instance, chemically exfoliated MoS_2 layers may lose their semiconducting properties due to structural changes induced by Li intercalation [113]. Liquid phase exfoliation often leads to a dispersion of flakes characterized by varying lateral sizes and thicknesses. This inherent heterogeneity poses a significant challenge for practical applications and represents a major impediment to the widespread industrial adoption of this technique.

Photoexfoliation is a cutting-edge technique in materials science. Employing the fundamental principles of light–matter interactions, photoexfoliation relies on the controlled absorption of photons to induce localized heating and subsequent exfoliation of thin layers from bulk materials [114, 115]. The process starts by obtaining a bulk crystal of a layered material, such as TMD. A laser beam, often in the visible or near-infrared spectrum, is focused onto the surface of the bulk TMD crystal. The energy from the absorbed laser light is transferred to the TMD crystal, causing localized heating and expansion. This sudden increase in temperature leads to a rapid vaporization of material, creating a high-pressure bubble beneath the surface. As the bubble expands and bursts, it exfoliates or cleaves a thin layer of TMD material from the bulk crystal [116, 117].

The exfoliated monolayer or few-layer TMD sheets are released into the surrounding environment, where they can be collected on a substrate placed nearby or dispersed in a suitable solvent to form a suspension. The obtained TMD monolayers can be characterized using various techniques to confirm their quality and thickness. This method offers a novel means of achieving monolayer or few-layer materials with tailored properties, revolutionizing the landscape of 2D materials research [118, 119]. Photoexfoliation provides excellent control over layer thickness and quality [120, 121].

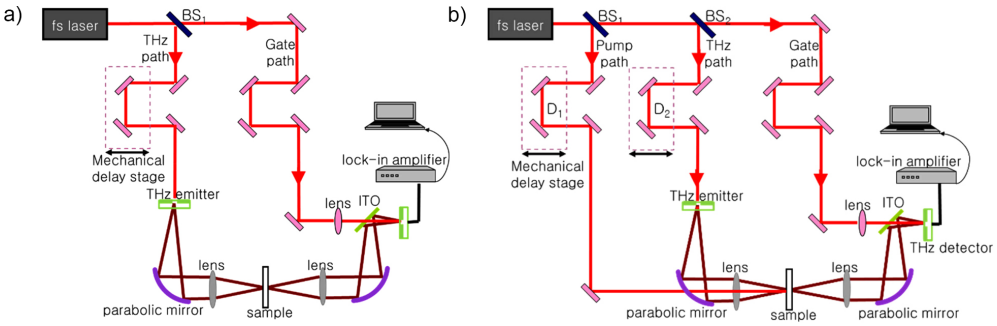

Figure 4. Schematic of common THz spectroscopic systems: (a) THz-TDS and (b) OPTP. An additional delay stage is present in the pump path in OPTP spectroscopy. Reprinted with permission from [131]. Copyright 2017, IOP Publishing.

3. Characterization of 2D Materials at THz Frequencies

3.1. Terahertz time-domain spectroscopy (THz-TDTS)

Terahertz time-domain spectroscopy (THz-TDS) is a powerful technique that has gained prominence in recent years for its ability to investigate materials and molecules in the THz frequency range, typically spanning from 0.1 to 10 THz [122, 123, 124, 125]. THz-TDS offers a unique window into the spectral region where electronic and vibrational transitions of molecules and materials occur, providing valuable insights into their structural and dynamical properties [126].

Figure 4(a) shows a typical THz-TDS setup. The fundamental principle behind THz-TDS involves the generation of ultrashort pulses of terahertz radiation and their subsequent detection, allowing for the precise measurement of the amplitude and phase of the terahertz field as a function of time [127, 125]. A femtosecond laser pulse is focused on a nonlinear crystal. The intense laser pulse induces a nonlinear response in the crystal, generating terahertz radiation. The pulse is then sent through a beam splitter, creating a reference pulse and a sample pulse. The sample under investigation is placed in the path of the sample pulse. The terahertz radiation interacts with the sample, and its properties influence the pulse in terms of absorption, reflection, and transmission. The altered sample pulse and the reference pulse (the gate path in Figure 4(a)) are sent to a detector, where the electric field of the pulses is measured as a function of time. The detector can be a photoconductive antenna, electrooptic crystal, or other devices sensitive to terahertz radiation. The time-domain signal obtained from the detector is then Fourier-transformed to obtain the frequency-domain spectrum. The resulting spectrum represents the absorption or reflection characteristics of the sample at different terahertz frequencies. The obtained spectrum provides information about the sample's dielectric properties, including absorption peaks related to vibrational and rotational modes. This temporal-domain approach facilitates the extraction of valuable information about a material's dielectric, refractive, and absorptive properties [128, 129, 130, 17].

The versatility of terahertz time-domain spectroscopy has led to its adoption in numerous diverse fields from investigation of the electronic properties and lattice dynamics, such as phonon resonances, intermolecular vibrations, and electronic transitions [124, 132] to studying biomolecules and their interactions [133, 134], and

security and quality control applications such as concealed weapons or drug detection.

THz-TDS offers a direct method for extracting the complex equilibrium conductivity from experiments. This is typically achieved through a transmission measurement approach, where a THz pulse $E(t)$ is directed onto the sample, and the resulting transmitted pulse $E_{\mathrm{sam}}(t)$ is observed. The sample, in this context, is the 2D material grown or transferred onto a substrate.

As the THz pulse traverses the sample, it undergoes absorption and delay due to interactions with both the sample and the underlying substrate. To isolate the contribution of the sample, a reference pulse E_{sub} is measured, representing the response of the substrate without the sample. The Fourier transform of these signals yields the transmission function $T(\omega) = \frac{E_{\mathrm{sam}}(\omega)}{E_{\mathrm{sub}}(\omega)}$.

Under the thin film approximation, which holds true for 2D materials, the complex conductivity $\sigma(\omega)$ is determined as described by Lloyd-Hughes and Jeon [135],

$$\sigma(\omega) = \frac{n+1}{Z_0}\left(\frac{E_{\mathrm{sub}}(\omega)}{E_{\mathrm{sam}}(\omega)} - 1\right), \tag{1}$$

where $Z_0 = 377\ \Omega$ is the free space impedance and n is the refractive index of the substrate. n can be treated as frequency-independent as most substrates exhibit dispersionless optical properties in the THz range.

3.2. Optical pump–probe (OPP) THz spectroscopy

Optical pump–probe (OPP) terahertz spectroscopy is a versatile pump–probe technique that combines elements of both ultrafast laser spectroscopy and THz spectroscopy to study the dynamics of photoexcited carriers in materials [46, 47]. This powerful method is employed to investigate the dynamics of a wide range of materials and systems, offering valuable insights into their electronic and vibrational properties on ultrafast timescales [47, 48].

In this technique, the pump pulse is used to excite a sample by temporarily altering its electronic or vibrational states. The pump pulse typically has a duration on the order of femtoseconds and can be tuned to specific wavelengths corresponding to electronic transitions in the material. The pump pulse excites carriers in the material by promoting electrons to higher energy states, creating electron–hole pairs (excitons) or other charge carriers. This perturbation generates a transient response in the material, leading to changes in its optical properties. The probe pulse is then introduced with a controlled time delay after the pump pulse. By measuring the change in the probe pulse intensity or phase, system response to the initial excitation is recorded [136, 137]. The probe pulse is sensitive to the changes induced by the pump pulse, such as alterations in the sample's dielectric properties caused by the presence of photoexcited carriers. The delay between the pump and probe pulses can be precisely controlled, allowing the study of the ultrafast processes and dynamics that occur within the material. The time-domain signal is Fourier-transformed to obtain the frequency-domain spectrum. The resulting THz spectrum provides information about the dynamics of carriers, including their mobility, recombination rates, and other relevant parameters. The obtained data can be analyzed to extract various material parameters, such as carrier lifetimes, mobility, and the influence of external factors (e.g., temperature, doping) on carrier dynamics.

The key innovation of OPP THz spectroscopy lies in its ability to capture the ultrafast and often complex dynamics of various systems, such as charge-

carrier recombination in semiconductors, structural changes in biomolecules, or phase transitions in materials [138]. As a result, this technique has found applications in physics, chemistry, materials science, and biology, offering new avenues for understanding the behavior of matter at the picosecond to femtosecond timescales.

3.3. Optical pump THz probe (OPTP) spectroscopy

Optical pump terahertz probe (OPTP) spectroscopy is a time-resolved technique designed to investigate photoinduced carrier dynamics. It quantifies the change in conductivity, $\Delta\sigma(\omega)$, arising from photoinduction. In this method, the sample undergoes photoexcitation induced by an above-bandgap optical pulse, followed by probing using a THz pulse. The time elapsed between the photoexcitation pulse and the peak of the THz pulse is referred to as the pump–probe delay. A typical setup is depicted in Fig. 4(b).

To establish a baseline, a reference measurement is conducted without photoexcitation. The alteration in transmitted electric fields, denoted as $\Delta E(t) = E_{\mathrm{sam}}(t) - E^0_{\mathrm{sam}}(t)$, where $E_{\mathrm{sam}}(t)$ represents the electric field with photoexcitation and $E^0_{\mathrm{sam}}(t)$ denotes the electric field without photoexcitation, is directly correlated with $\Delta\sigma(t)$. Following Fourier transformation, under the thin film approximation, this relationship is expressed as:

$$\Delta\sigma(\omega) = -\frac{n+1}{Z_0}\frac{\Delta E(\omega)}{E^0_{\mathrm{sam}}(\omega)} \tag{2}$$

The detailed methods for extraction are described in previous reviews [139, 140, 141, 142].

3.4. Benefits of THz spectroscopies in characterizing 2D materials

Terahertz spectroscopies provide a distinctive path to observing novel phenomena in 2D materials. As shown in Figure 1(b), single-particle and collective electron excitations, as well as vibrational and phonon excitations, occur in this frequency range. For example, OPTP on TMDs revealed the layer-dependent influence of exciton and trion formation [71]. Moreover, THz spectroscopies provide insights into ultrafast physics phenomena that are difficult to access using other methods, such as the effects of synthesis and processing. For example, the change in the sign of graphene photoconductivity due to substrate impurities was first observed in THz spectroscopic studies [143, 144]. MXenes showed distinct carrier dynamics before and after annealing owing to the reduction of internanosheet distance, as observed in OPTP measurements [145]. While frequency-domain techniques, such as far-IR Fourier-transformed infrared spectroscopy (FTIR), have also been used in the THz range, they suffer from a low signal-to-noise ratio [146]. Finally, not only do THz spectroscopies capture intraband transitions, they are also highly versatile in investigating high-temperature processes, many-body effects, and nonlinear THz effects [146, 18]. THz time-resolved characterization also provides direct observation of complex conductivity spectrum without using the Kramers-Kronig relation [147].

4. Conductivity Models

4.1. Phenomenological models

The frequency-dependent complex conductivity $\sigma = \sigma_1 + i\sigma_2$ extracted from experiments provides insights into carrier transport in 2D materials. Often, experimental data is fitted with simple phenomenological models, such as the Drude model and its expanded forms, including the generalized Drude model, Drude–Smith model, and Drude–Smith–Lorentz model. These models may offer reasonable representations of the observed conductivity spectrum, depending on the governing transport process of the material. However, in cases where many-body interactions prevail, these simpler conductivity models may prove inadequate.

The Drude model describes the electrical properties of conductors where the dominant scattering mechanism for charge carriers is energy-independent or weakly energy-dependent. The Drude model characterizes the conductivity [135, 140] as

$$\sigma(\omega) = \frac{\sigma_{\mathrm{dc}}}{1 - i\omega\tau}, \tag{3}$$

where ω is the angular frequency, τ is the effective momentum-relaxation time [148], sometimes referred to simply as the relaxation time or scattering time, and σ_{dc} is the dc conductivity. Experimentally, however, it is convenient to write the Drude conductivity as

$$\sigma(\omega) = \frac{\mathrm{D}}{\Gamma}\frac{1}{1 - i\omega/\Gamma}, \tag{4}$$

where $\Gamma = 1/\tau$ is the relaxation rate (the inverse of the relaxation time) and $\mathrm{D} = \sigma_{\mathrm{dc}}\Gamma$ (sometimes also written $\mathrm{D} = \pi\sigma_{\mathrm{dc}}\Gamma$) as is the experimentally measured quantity known as the Drude weight.

It turns out that Drude model is well suited for the description of THz absorbance in 2D material with parabolic bands, such as TMDs. At THz frequencies, intraband (rather than interband) processes dominate, and the 2D materials' energy-independent density of electronic states results is energy-independent electron–phonon scattering rates and, consequently, Drude-like behavior [149].

While the simple Drude model is appropriate in 2D materials with parabolic electronic dispersion, for bulk semiconductors such as silicon [150] and GaAs [151], and nanomaterials such as suspended graphene [152], where the dominant scattering mechanism has a pronounced energy dependence, the generalized Drude model is more appropriate. This model reads

$$\sigma(\omega) = \frac{D}{\Gamma\left[1 - (i\omega/\Gamma)^{1-\alpha}\right]^{\beta}}, \tag{5}$$

where α and β are real-valued parameters ($0 \leq \alpha, \beta \leq 1$). For $\alpha = 0$ and $\beta = 1$, the generalized Drude model reduces to the simple Drude model.

However, in a wide range of 2D materials including TMDs, THz conductivity shows non-Drude trends owing to phenomena that go beyond the simple single-electron scattering picture.

The Drude–Smith model is an extension of the Drude model, where the Smith term incorporates backscattering. It was was introduced in [153, 154] as

$$\sigma(\omega) = \frac{\sigma_{\mathrm{dc}}}{1 - i\omega\tau}\left[1 + \sum_{n=1}^{\infty} \frac{c_n}{(1 - i\omega\tau)^n}\right], \tag{6}$$

where c_n are backscattering parameters that describe the memory effect of carrier velocity. While the Drude model describes isotropic carrier scattering, the Drude–Smith model is used to describe anisotropic scattering with a preferential direction. $c_n = 0$ indicates full anisotropic and elastic Drude scattering while $c_n = -1$ indicates complete suppression of conductivity due to backscattering. The infinite sum in Eq. (6) is often truncated to the first term, giving rise to a more commonly known form in literature:

$$\sigma(\omega) = \frac{\sigma_{\mathrm{dc}}}{1 - i\omega\tau}\left[1 + \frac{c}{1 - i\omega\tau}\right]. \tag{7}$$

The backscattering may be attributed to localization due to compositional inhomogeneity and alloy scattering [155, 156], polycrystallinity [157], or the characteristics of weakly confined systems [158, 159, 160]. An interpretation based on a diffusive restoring current has been proposed [161], modified from Eq. (7) and incorporating two different relaxation times. Modified Drude–Smith-like conductivity has also been suggested for semiconductor nanocubes and nanocrystals [162, 163].

In monolayer and few-layer materials, quasiparticles such as exctions and trions play a significant role in the THz conductivity [71]. The effect of excitonic and trionic resonances is included through the addition of Lorentz-type peaks in the Drude formula:

$$\sigma(\omega) = \sum_{m} \frac{\mathrm{D_m} i\omega}{\omega^2 - \omega_{0,m}^2 - i\omega\Gamma}. \tag{8}$$

Here, the subscript m accounts for different types of resonances and $\omega_{0,m}$ are the resonant frequencies. Similar terms can be added to the Drude–Smith model, resulting in the Drude–Smith–Lorentz model that captures both backscattering and resonant phenomena originating from multiparticle excitations.

4.2. Multiphysics models

Theoretical and computational work in the terahertz frequency range is limited. A major obstacle is the requirement to simultaneously consider electronic transport and electrodynamics, owing to the similar values of excitation frequencies and typical scattering rates. This alignment renders the frequently used quasistatic approach for electrodynamics inadequate. A multiphysics tool combining ensemble Monte Carlo (EMC) transport simulation, finite-difference time-domain (FDTD), and molecular dynamics (MD) has been employed to counter the challenge [164, 165, 149]. EMC is a particle-based stochastic semiclassical simulation technique where a large number of carriers are tracked over time as they drift and scatter under relevant scattering mechanisms. The technique can be used to efficiently simulate non-equilibrium carrier dynamics [166, 167]. EMC is widely used for simulating device physics at dc and in the low-frequency regime [168] under the quasistatic approximation for electromagnetic

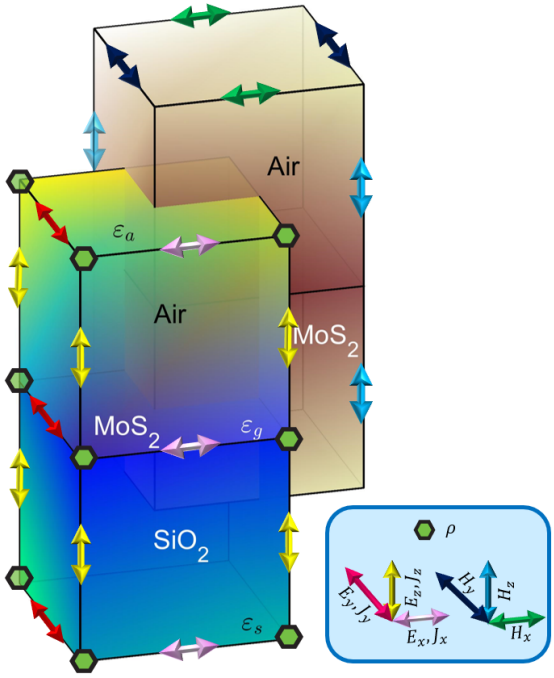

Figure 5. The Yee cell assignment of electric and magnetic fields **E** and **H**, charge density ρ, and current density **J** in an air/MoS_2/SiO_2 structure. The 2D material lies in the central plane, sandwiched between the half-spaces filled with air on top and substrate on the bottom. **E** and **H** fields are staggered in space. **E** is co-located with **J**. Charge density ρ, which does not commonly feature in pure FDTD implementations, must be incorporated in the coupled EMC–FDTD simulation.

fields. At terahertz frequencies, this assumption is not valid. That is where FDTD comes into play which delivers a full-wave solution of Maxwell's equations in a way that self-consistently couples to the transport solver [164, 169, 150, 165, 152, 149]. FDTD calculates the electric field **E** and magnetic field **B**, which is used to calculate Lorentz force **F** acting on the carriers and update the current density and position of the carriers using EMC. Figure 5 shows the staggered Yee-cell implementation of EMC–FDTD scheme for a layer of MoS_2 on top of SiO_2 substrate. The technique, along with the incorporation of MD for short-range sub-grid cell interaction, has been used to calculate THz conductivity of doped silicon [170, 169, 164, 150], graphene [165, 152, 171], and TMD MoS_2 [149].

4.3. Quantum models

The phenomenological models and multiphysics models described above incorporate semiclassical electronic transport, which, among other things, implies that interband transitions are neglected, which may be appropriate at THz frequencies in 2D materials. However, if interband transitions may not be neglected, then a quantum-electronic-transport picture becomes necessary. A common approach is to employ the Kubo–Greenwood linear-response formula with the relaxation-time approximation

(RTA) that compresses all scattering information into one effective relaxation time. A more accurate approach to quantum electronic transport that encompasses both full electronic dispersions and a detailed account of various dissipative mechanisms involves solving the Markovian master equation for the density matrix [172], and this technique has been used to calculate both linear and nonlinear response of graphene and TMD nanostructures [173, 174]. However, due to nonlocal screening effects in 2D materials, exciton and trions are also relevant in 2D materials in the THz frequency range, which we will discuss in detail in Sec. 5. In general, a solution to the Bethe-Salpeter equation (BSE) is required to treat many-body phenomena, and we refer interested readers to the review by Quintela *et al.* [175]. Perturbative approaches taking into accountg free-carrier, exciton, and trion contributions to conductivity while employing a phenomenological scattering rate have also been reported in 2D systems [176, 177, 178].

5. THz Response of 2D Materials

In this section, we first explore the effects of doping, charged impurities, substrate, and growth environment on THz-frequency carrier dynamics in graphene. Next, we examine the impact of free carriers, excitons, and trions on the carrier dynamics in TMDs and also highlight the significance of boundary and defect scattering in MXenes. Furthermore, we explore exciton–polaron interactions in perovskites and novel surface-state physics in topological materials.

5.1. Graphene

Ever since the discovery of graphene [1], significant attention has been devoted to exploring its optoelectronic [179], plasmonic [180, 181], and THz [182, 183, 184] properties. In the THz range, optical absorption in graphene arises from free-carrier intraband transitions, aligning with the traditional Drude model [143, 68, 185, 186, 67, 187]. Experimental studies based on Fourier-transform infrared spectroscopy (FTIR) have concluded that the gate-dependent ac near-equilibrium conductivity of graphene is primarily governed by intraband transitions, leading to free-carrier absorption and scattering at various doping densities.

Despite the consistency of these experimental findings, discrepancies emerged when the measured Drude weight (denoted as $D_0 = 2\pi E_F/\hbar$) was compared with calculations based on the random-phase approximation (RPA) at 0 K. Possible factors such as short-range electron–electron interaction [188], localized impurity distribution [189, 190], and theoretical predictions of higher-than-D_0 Drude weight [191] were considered. Subsequent macroscopic multiphysics simulations shed light on the reduction of the Drude weight, attributing it to a combination of substrate impurity–electron interaction, electron–electron interaction, and clustered impurity distribution [165, 171]. To achieve a good fit for $\sigma(\omega)$, the use of the generalized Drude model in Eq. (5) became necessary.

Figures 6(a)–6(c) depict the real part of $\sigma(\omega)$ as a function of THz frequency. Notably, the reduced conductivity observed at low THz frequencies aligns well with experimental data obtained from references [67, 68, 192] when fitted using the generalized Drude model. In Fig. 6(d), the dominant scattering process is illustrated as the impurity density increases: at low impurity densities, scattering is predominantly influenced by phonon scattering with strong spin-orbit coupling, while

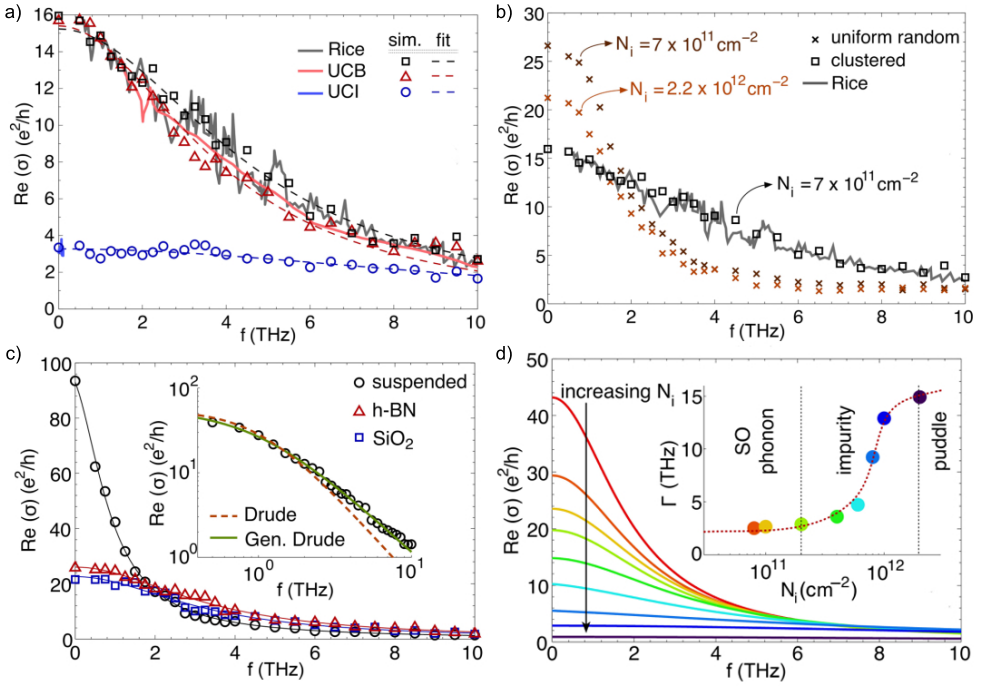

Figure 6. (a) Real part of $\sigma(\omega)$ calculated using EMC–FDTD–MD simulation and matched against experimental results from [67, 68, 192]. (b) A clustered distribution of impurities is needed to explain the low conductivity obtained in experiment. (c) The generalized Drude model best fits to the experimental data for graphene on top of hBN and SiO_2 substrates. (d) As the impurity density increases, the dominant scattering mechanism changes from SO phonons to clustered impurities, and lowers the conductivity. Reprinted with permission from N. Sule, K. J. Willis, S. C. Hagness, and I. Knezevic, Phys. Rev. B 90, 045431 (2014) [152]. Copyright (2014) by the American Physical Society.

higher impurity densities lead to the formation of electron–hole puddles dictating conductivity.

THz-TDS measurements have shown a sheet conductivity of large-area graphene films grown by CVD that is thirty times larger than that observed at visible wavelengths [193]. This enhancement is attributed to the dominance of intraband processes.

The growth environment plays a key role in THz performance of graphene structures kept in a low-humidity environment, as shown by Maeng *et al.* [194]. When modifying carrier density via electrostatic gating, for the Fermi energy close to the Dirac point, sheet conductivity was shown to be dependent on temperature, not carrier density. Far from the Fermi energy, conductivity changes $\propto \sqrt{N}$, with N being the carrier density. In contrast, a study by Buron *et al.* kept the sample in atmospheric conditions with ample O_2 and H_2O, and the work showed linear dependence with gate voltage [195]. This is because the gas adsorption process produces p-type graphene where transport is dominated by long-range impurity scattering. A semiclassical Kubo-based formalism that takes free-carrier intraband processes into account often provides an accurate representation of single-layer and few-layer graphene sheets [196].

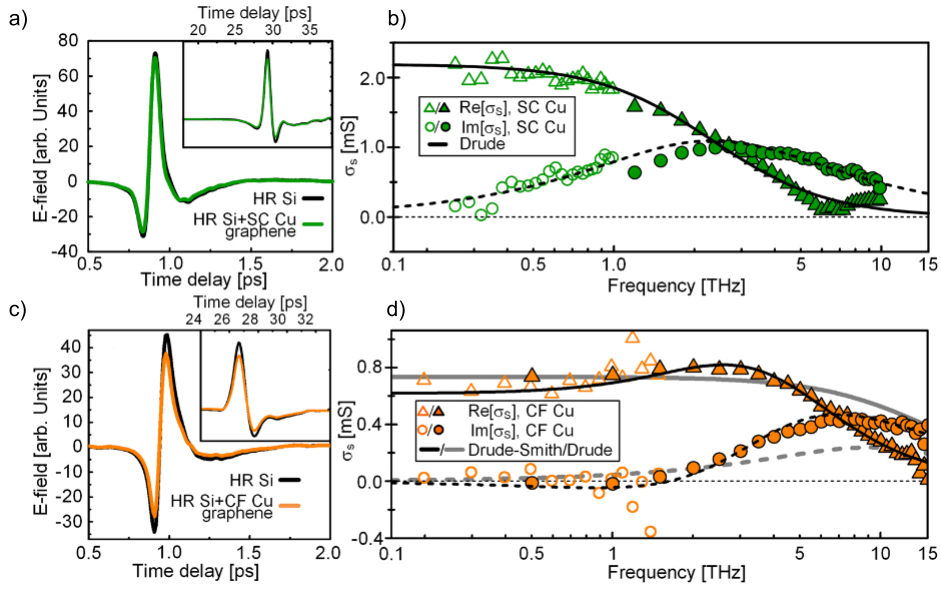

Figure 7. (a),(c) Ultrawideband THz signal used in THz-TDS experiment of single crystal (SC) Cu (green) and copper foil (CF) Cu (brown) grown graphene. (b) The real part (triangles) and imaginary part (circles) of σ_s SC-grown graphene show traditional Drude fitted conductivity (d) CF-grown graphene shows the Drude-Smith type response indicating the onset of boundary scattering. Reprinted with permission from [69]. Copyright 2014, American Chemical Society.

Nonetheless, there are specific instances where the Drude model falls short, as it fails to explain experimental observations that demonstrate a reduction in surface conductivity at dc and low frequencies. In a study conducted by Buron *et al.*, graphene was grown on single-crystalline (SC) and commercial-foil (CF) copper substrates, then transferred onto a SiO_2 substrate [197, 69]. While the graphene grown on SC-Cu exhibited traditional Drude behavior, as shown in Fig. 7(a),(b), the sample grown on CF-Cu showed non-Drude behavior, specifically following the Drude–Smith model, as in Eq. 7, shown in Fig. 7(c),(d). The origin of this behavior is attributed to the localization (stemming from pronounced back-scattering) of carriers in the commercial disordered ("dirty") metals. The non-Drude conductivity is also evident in graphene grown on metal-backed polymer substrates [198], graphene [199], reduced graphene-oxide [200], and 3D graphene aerogels [201].

The nonequilibrium photoconductivity of graphene, typically studied through the optical-pump terahertz-probe (OPTP) technique, has undergone extensive investigation. Early studies on ultrafast carrier dynamics in graphene revealed a reduction in THz conductivity after photoexcitation [202, 203]. This negative photoconductivity suggests a population inversion process near the Dirac point, leading to stimulated emission—a phenomenon crucial for potential graphene lasers.

Subsequent studies by Frenzel *et al.* [204, 205], Jnawali *et al.* [206], and Tielrooji *et al.* [207] also observed negative photoconductivity. However, the origin of this phenomenon was attributed to secondary hot-carrier generation [207].

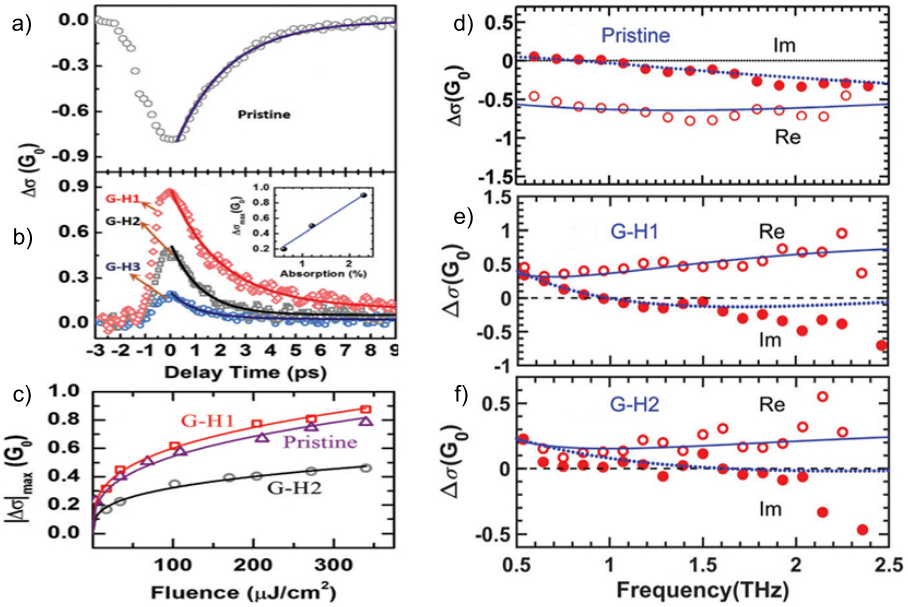

Figure 8. (a) The transient photoconductivity $\Delta\sigma(t)$ is depicted for (a) pristine and (b) Hydrogenated graphene samples. C/H ratio of the samples G-H1, G-H2, and G-H3 is 19 %, 25%, and 29% respectively. (c) $|\Delta\sigma_{\max}|$ plotted against fluence, ϕ where $|\Delta\sigma_{\max}| \sim \phi^{1/3}$. The photoinduced conductivity spectra $\Delta\sigma(\omega)$ fitted for (d) pristine graphene as well as (e) G-H1 and (f) G-H2 graphene samples under a pump fluence of 340 μJ/cm^{-2}. $\Delta\sigma(\omega)$ shows negative to positive transition as hydrogen content increases. Reproduced with permission from [70]. Copyright 2018, Royal Society of Chemistry.

Photoexcited carriers interact with doped carriers via carrier–carrier scattering, generating secondary hot carriers. These hot carriers are rapidly neutralized by Auger recombination, resulting in unsustainable population inversion. The interplay between scattering rate and Drude weight has been identified as a contributing factor to the negative terahertz photoconductivity. The photoconductivity, expressed as $\Delta\sigma/\sigma = \Delta D/D - \Delta\Gamma/\Gamma$, becomes negative when the increase in scattering in the second term dominates the change in the Drude weight in the first term.

Kar *et al.* [70] observed a transition from negative to positive photoconductivity in hydrogenated graphene (Fig. 8) to a bandgap opening and a shift in the Fermi energy. Tomadin *et al.* [208] attributed this transition to an increase in free carrier density and a rise in electron temperature. Docherty *et al.* [209] demonstrated that p-doped CVD-grown graphene exhibits positive photoconductivity in O_2 and negative photoconductivity in an N_2-rich environment. The negative photoconductivity in a gaseous environment was attributed to a small band gap (∼8 meV) opening near the Dirac point after gas adsorption, which alters the linear density of states of pure graphene and lowers the photoconductivity.

5.2. TMDs

In contrast to graphene, which has linear electronic band dispersion and no bandgap, TMDs in monolayer and multilayer forms possess direct and indirect bandgaps, respectively. TMDs can be thinned down through mechanical and chemical exfoliation, and synthesized into single and multilayers using methods such as CVD and MOCVD. In monolayer TMDs, a transition-metal layer is sandwiched between two layers of chalcogens. Multilayer TMDs are formed by stacking trilayers, which are held together by the weak van der Waals forces. Depending on the transition metal involved, TMDs can exhibit semiconducting, metallic, semimetallic, or insulating properties. Common TMDs include atomically thin MoS_2, $MoSe_2$, $MoTe_2$, WS_2, and WSe_2, which have been extensively studied for their interesting optoelectronic properties [210, 211, 212].

Most time-resolved pump-probe experiments investigating the ultrafast carrier dynamics in TMDs have actually involved OPTP [213, 214]. As OPTP requires light excitation above the bandgap, these studies are primarily focused on the exciton and trion dynamics [215]. A more comprehensive understanding of free carriers and their role in the equilibrium ac conductivity of TMDs is crucial, and simulations can shed valuable insight on this issue. Figure 9 shows the simulation results, obtained using the multiphysics EMC–FDTD technique discussed in [149, 165], for the terahertz ac conductivity of single-layer TMDs that are suspended (Fig. 9(a)) and supported (Figs. 9(b)–(d)) on commonly used substrates hBN, Al_2O_3, and SiO_2 [216]. Carrier scattering with acoustic phonons, optical phonons (both nonpolar and polar aspects of such scattering), impurities, and surface optical phonons are considered in the simulation. Monolayer TMDs are quasi-2D direct-bandgap materials with nearly parabolic bands and isotropic effective mass m^* at the K point. This translates to energy-independent terahertz scattering rates at low electron energies for a number of mechanism where the rate is proportional to the density of states. While in the suspended case there is no dominant scattering mechanism, for supported TMDs the dominant SO phonon scattering lies in the higher THz range. For electron density of 5×10^{12} cm^{-2} and impurity density of 1×10^{12} cm^{-2}, which are reasonable values based on experiments, the calculation shows higher low-frequency conductivity of suspended layers without any SO phonon scattering than for layers supported on substrates. hBN is less polar than SiO_2 and Al_2O_3, and, consequently, TMD electrons have a lower scattering rate with SO phonons on hBN than on the other two polar substrates. Overall, the free-carrier contribution to THz conductivity in TMDs shows Drude-like behavior as the dominant mechanisms have energy-independent rates, which mathematically leads to a Drude-type conductivity [149]. The fitting parameters for the Drude model can be found in Table 1. While the Mo-based TMDs have comparable conductivities, W-based TMDs have a slightly higher conductivity thanks to the lower m^*. The results can be interpreted as the conductivity of pristine TMDs without grain boundaries, so no grain-boundary-induced backscattering is present. The simulation results may aid in the effort to understand THz-frequency near-equilibrium free-carrier electronic transport in TMDs on different substrates and having different impurity densities.

The characteristics of photoexcited TMDs differ significantly from those where carriers are near equilibrium. In the context of single-layer TMDs, the primary influence on their physical characteristics stems from the Coulomb interaction among carriers. This effect is particularly pronounced due to reduced dielectric screening, which enables exciton excitation even at room temperature. MoS_2 stands out as the

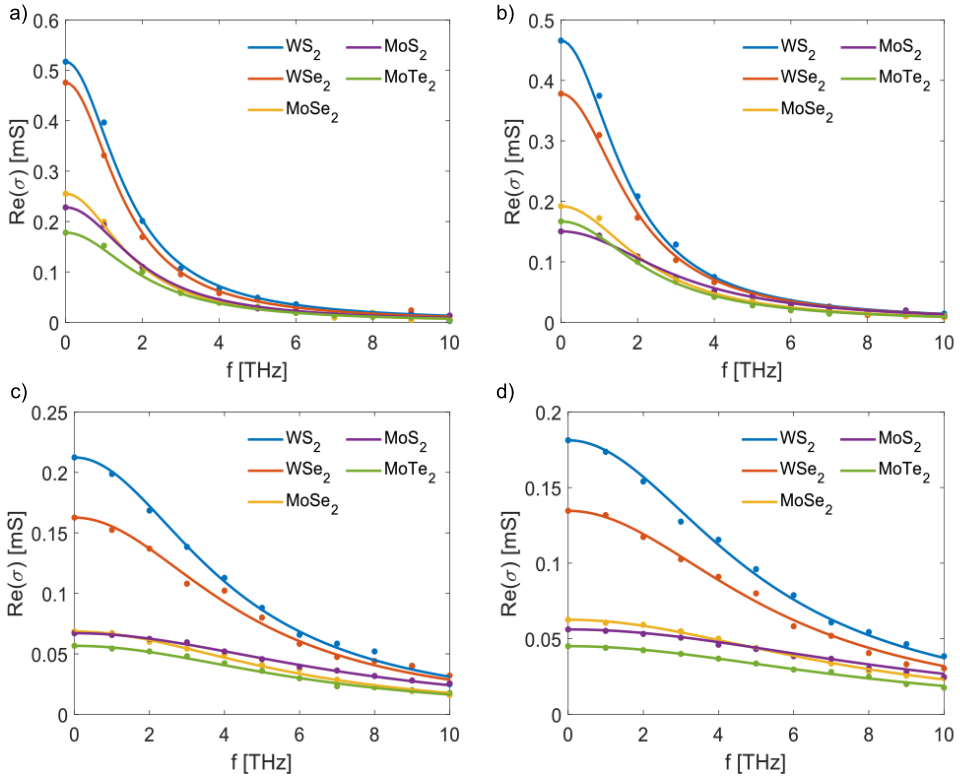

Figure 9. Real part of $\sigma(\omega)$ as a function of THz frequency of MoS_2, $MoSe_2$, $MoTe_2$, WS_2, and WSe_2 (a) suspended (without substrate), supported on (b) hBN, (c) sapphire (Al_2O_3), and (d) SiO_2 substrate. The electron density and impurity density through the simulation is 5×10^{12} cm^{-2} and 1×10^{12} cm^{-2} respectively. The dots correspond to conductivity calculated from EMC-FDTD simulation [149]. Solid lines are Drude fits, with the parameters given in Table 1.

most researched TMD, especially notable for its potential optoelectronic applications following the observation of a giant enhancement in photoluminescent (PL) emission.

The first study of THz photoconductivity of TMDs was conducted by Docherty *et al.* [71] in 2014 using the OPTP technique. The authors' ultrafast transient study of CVD-grown monolayer MoS_2 revealed the ultrafast quenching of PL, independent of the type of resonant carriers. This phenomenon was attributed to fast recombination with high-density surface trap states. Figures 10 (a) and (b) show the photoconductivity of monolayer and trilayer MoS_2, respectively. The authors reported positive real and negative imaginary parts of the photoconductivity, which is reasonable when a restoring force on carriers is present, or there is a resonance with excitons or plasmons. Monolayer MoS_2 with a trion binding energy of ∼18 meV (4.5 THz) exhibited a trion resonance according to a fit of the conductivity with the Drude–Lorentz model (Eq. (8)). Trilayer MoS_2, lacking trion mode but with an exciton binding energy of ∼100 meV, did not exhibit trion resonance.

Lui *et al.* [217] performed OPTP measurements of CVD-grown monolayer MoS_2 with an 400-nm pump pulse. Figure 10(d) shows the time-resolved normalized THz waveform $\Delta E(t)_{max}/E(t)_{max} (\propto -\mathrm{Re}(\Delta\sigma))$ exhibiting a fast relaxation time of 1 ps

Table 1. Drude-fit parameters for various 2D materials and substrates obtained from EMC–FDTD [149]

Material	Substrate	σ_{DC} (mS)	τ (fs)
MoS_2	–	0.2280	80.00
	hBN	0.1504	51.28
	Sapphire	0.0671	21.28
	SiO_2	0.0562	16.67
$MoSe_2$	–	0.2552	90.91
	hBN	0.1920	68.97
	Sapphire	0.0685	27.03
	SiO_2	0.0626	20.83
$MoTe_2$	–	0.1779	76.90
	hBN	0.1669	66.67
	Sapphire	0.0566	25.00
	SiO_2	0.0451	18.87
WS_2	–	0.5171	99.01
	hBN	0.4658	90.91
	Sapphire	0.2124	38.46
	SiO_2	0.1813	31.25
WSe_2	–	0.4755	96.01
	hBN	0.3780	83.33
	Sapphire	0.1626	34.48
	SiO_2	0.1346	28.57

and subsequently a long relaxation time of 42 ps. Figure 10(e) shows the complex conductivity for the probe time delay of 3 ps and 40 ps. In contrast to the observation of Docherty *et al.*, both the real and imaginary parts of the photoconductivity were negative. The authors attributed this phenomenon to the formation of negative trions (two electrons and one hole quasiparticle). The presence of negative trions, with a higher effective mass ($m_T^* = 2m_e^* + m_h^*$), leads to reduced mobility. Nevertheless, a complete understanding of the origin of negative and positive conductivity remains unclear, necessitating further theoretical efforts.

Subsequently, Cunningham *et al.* [218] conducted OPTP measurements on CVD-grown monolayer MoS_2. The authors reported a positive real part and negligible imaginary part of $\Delta\sigma$, indicating no trion resonance. The absence of trions was suggested to result from O_2 neutralization at grain boundaries during the growth process. The photoconductivity was fitted using the Drude–Smith model, suggesting the presence of carrier backscattering and grain boundaries.

For multilayer MoS_2, Kar *et al.* [219] characterized 5–6 layer samples via OPTP. The carrier dynamics were reported to be dominated by Auger-assisted scattering involving electrons, holes, and excitons. In a study by Strait *et al.* [220], OPTP spectroscopy was performed on multilayer MoS_2 at different temperatures. Below 200 K, the Drude conductivity was reported to be limited by acoustic phonons, while at high temperatures, the conductivity was limited by optical phonons.

Several studies have been conducted on tungsten-based TMDs. Docherty *et al.* [71] first investigated THz response of monolayer WS_2 which showed a fast photoexcitation ($\tau \sim 1$ ps) followed by a slow decay ($\tau \sim 15$ ps) process as shown in

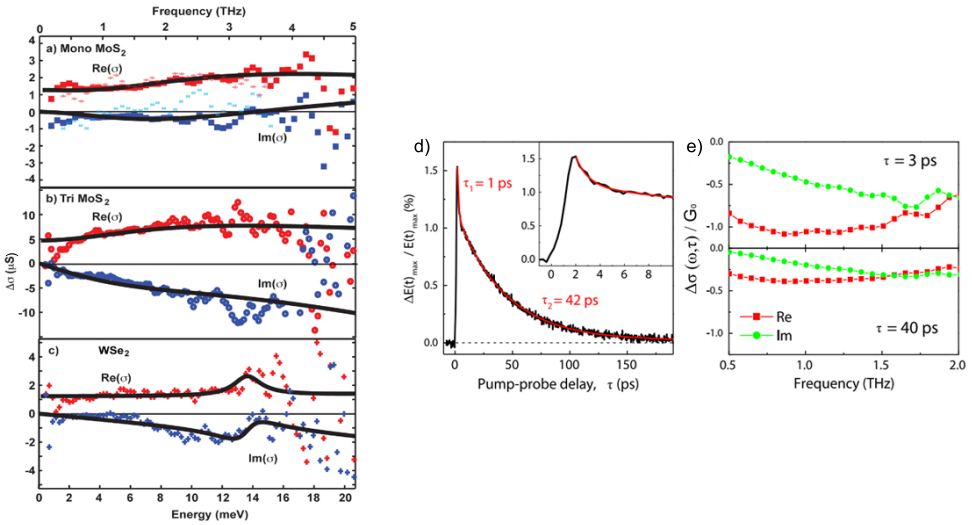

Figure 10. THz photoconductivity ($\Delta\sigma$) spectra for various monolayer and multilayer TMDs. (a) Monolayer MoS_2, 1.5 ps after photoexcitation with 3 eV (squares) and 1.9 eV (crosses) photons. The resonance at 18 meV is attributed to trions. (b) Trilayer MoS_2 1.5 ps after photoexcitation by 1.9 eV photons. It does not show tronic resonance in the THz range, but has an exciton resonance around 100 meV. (c) Monolayer WSe_2 excited with 1.65 eV photons, 1 ps after photoexcitation shows a clear A excitonic resonance. Reprinted with permission from [71]. Copyright 2014, American Chemical Society. (d) Temporal evolution of the ratio of $\Delta E(t)_{max}/E(t)_{max}$ fitted with a bi-exponential (red line) yields a short and a long lifetime, $\tau_1 = 1$ ps and $\tau_2 = 42$ ps, respectively. The long component emerges as the primary contributor to the overall dynamic response in the high-fluence regime. (e) Negative $\Delta\sigma(\omega)$ throughout the whole THz range at $\tau = 3$ and 40 ps for the pump fluence of 50 $\mu J/cm^{-2}$ and photon energy 3.1 eV. Reprinted with permission from C. H. Lui, A. J. Frenzel, D.V. Pilon, Y.-H. Lee, X. Ling, G. M. Akselrod, J. Kong, and N. Gedik, Phys. Rev. Lett. 113, 166801 (2014) [217]. Copyright (2014) by the American Physical Society.

Fig 10(c). However, the study had low signal-to-noise ratio. Later, a study by Xu *et al.* [221] shed more light on carrier transport. Photoconductivity fitted with the Drude–Smith model indicated carrier localization dominated by exciton formation, Auger recombination, and surface trapping. They could not detect exciton and trions. Dong *et al.* [223] showed that substrate-induced disorder facilitates the carrier localization process. In contrast, Gustafson *et al.* [222] reported the first measurement of trion binding energy in monolayer WS_2 at round 7.5 THz. They modeled the photoconductivity as the sum of three components: a Drude component, a broad-resonance component, and a dissociation-of-trions component. Figure 11 shows the photoconductivity of monolayer WS_2. Figures 11(a) and 11(b) show the Drude–Smith type conductivity for different pump fluences at $\tau_p = 1$ ps and $\tau_p = 3$ ps, respectively [221], and Fig. 11(c) shows the trion contribution to photoconductivity [222]. The discrepancy between the studies may stem from the former study having a narrow frequency range (below 7 THz) while the latter had a much broader frequency range to capture the trion effects.

Finally, bulk WSe_2 OPTP measurement revealed the presence of free carriers and excitons simultaneously [224]. As a result, photoconductivity was fitted with the

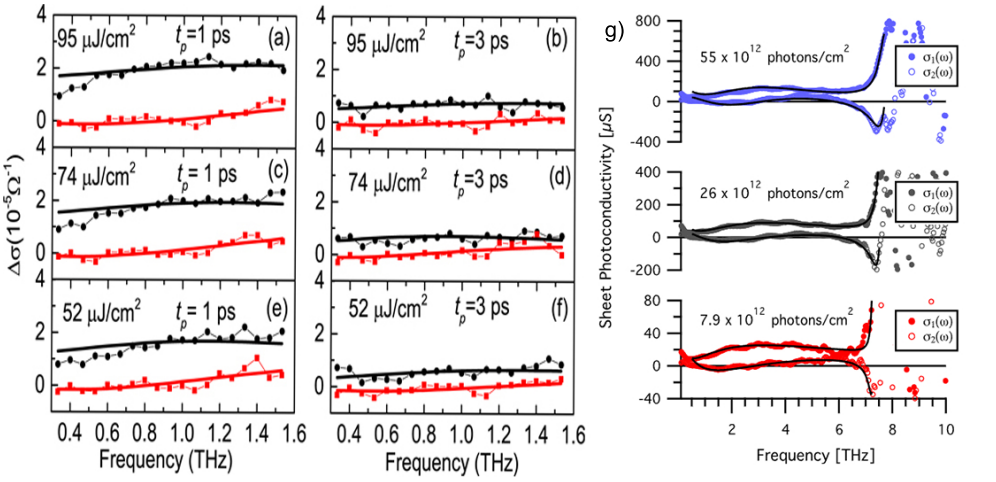

Figure 11. Complex photconductivity of monolayer WS_2 at pump delays of (a) 1 ps and (b) 3 ps, utilizing a pump fluence of 95 μJ/cm^{-2}. Similarly, at pump delay of (c) 1 ps and (d) tp = 3 ps with a pump fluence of 74 μJ/cm^{-2} (e) at 1 ps and (f) 3 ps at a pump fluence of 52 μJ/cm^{-2}. The pump-pulse wavelength is 400 nm. Experimental data (dots and circles) are fitted with the Drude–Smith model (solid curve). Reproduced with permission from [221]. Copyright 2019, IOP Publishing. (g) Complex photconductivity at various fluences for a monolayer WS_2 sample pumped at resonance (557 nm) with A exciton at 20 K and probed after 0.4 ps. The jump at 7 THz corresponds to a trion resonance. Reprinted with permission from [222]. Copyright 2019, American Chemical Society.

Drude–Smith–Lorentz model. Authors identified the fast phonon-assisted processes and the slow defect-assisted processes as the main decay mechanisms, and grain size and polycrystallinity of the sample played important roles [225].

5.3. MXenes

MXenes represent a novel category of 2D materials comprising transition metal carbides, nitrides, carbonitrides, and borides, and are characterized by the formula $M_{n+1}X_nT_{z\,(\text{or }x)}$. In this formula, M stands for a transition metal such as Sc, Ti, Zr, Hf, V, Nb, Ta, Cr, Mo, while X is either carbon, nitrogen, or boron, and n can be 1, 2, 3, or 4. The Tz component signifies surface termination, which can include groups like -OH, -O, and/or -F [226]. The name MXene originates from their primary method of synthesis, which involves the selective etching of the A-group elements (predominantly aluminum) from their parent MAX phases. Presently, more than 70 stable varieties of MXenes have been theoretically predicted, and upwards of 30 have been successfully created in laboratory settings [227]. Among them, bulk $Ti_3C_2T_x$ has conductivity as high as 20,000 Ωcm^{-1} [228], which results in a strong absorption across the THz range and makes it a promising new material for electromagnetic shielding and THz detectors [229, 230, 231].

THz-TDS studies conducted by Li *et al.* [232] on a continuous 25-nm-thick and a discontinuous 16-nm-thick film of $Ti_3C_2T_x$ showed intrinsic THz dc conductivity on the order of $\sim$ 1100 Ωcm^{-1}. The analysis revealed that both films exhibit suppressed conductivity at low frequencies, which was attributed to carrier transport being hindered by carrier localization at boundaries between nanoflakes. This effect was

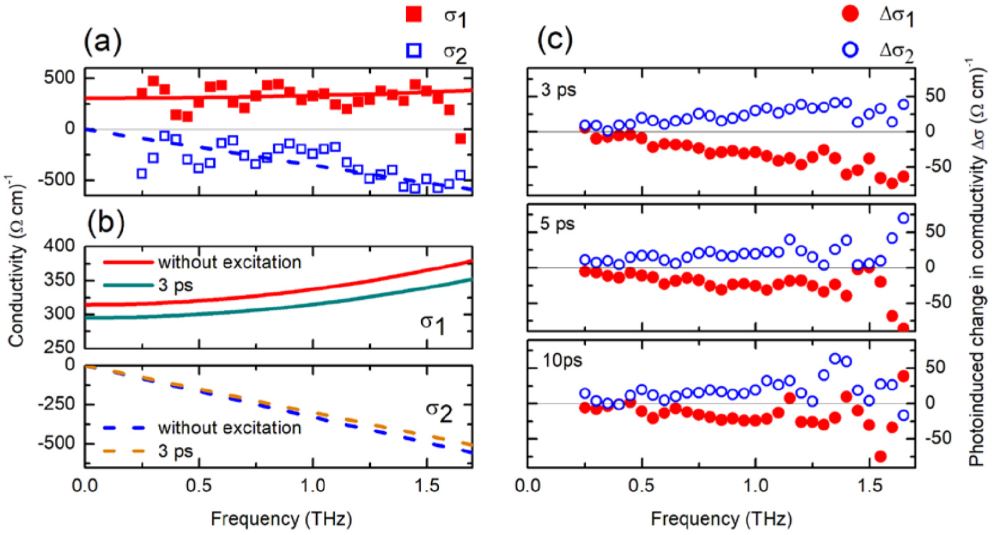

Figure 12. (a) THz sheet conductivity of a 16-nm $Ti_3C_2T_x$ film excited by a pulse of fluence 280 $\mu J/cm^{-2}$ and 800 nm wavelength. (b) Drude–Smith fits without excitation (as shown in (a)) and 3 ps after excitation. Suppression of the real part and the negative imaginary part of the conductivity indicate carriers constrained over mesoscopic lengths owing to nanocrystalline barriers and granularity of the sample. (c) THz photoconductivity at different times after excitation. Negative photoconductivity for all cases indicates metallic behavior of the material, with an increase of boundary scattering. Reproduced with permission from [232]. Copyright 2018, IOP Publishing.

modeled using the Drude–Smith model, as shown in Figs. 12)(a) and (b), and the model emphasizes the impact of defects and barriers like nanoflake edges on carrier transport. The continuous film, with larger overlapping flakes, showed higher dc conductivity and a less negative Drude–Smith c-parameter than the discontinuous film. The study also showed that film morphology, particularly the size and overlap of individual flakes, plays a crucial role in film conductivity, with larger nanoflakes in uniform films being preferable for applications requiring high MXene conductivity. A more recent study by Li *et al.* [233] indicated that substrate scattering dominates for monolayer samples while many-layer samples show reduced substrate dependence due to dielectric screening effect.

OPTP measurement with 400 nm and 800 nm wavelength excitation on the 25 nm sample revealed sustained negative photoconductivity over several picoseconds. Figure 12(c) shows the negative photoconductivity for 800 nm pulse. The authors attributed this phenomenon to increased scattering due to the increased temperature of the hot carriers generated via the interband transitions following above-bandgap excitation.

MXenes containing molybdenum, such as $Mo_2Ti_2C_3T_z$ and $Mo_2TiC_2T_z$, where some titanium atoms are substituted by Mo, show reduced overall conductivity stemming from difficult inter-nanosheet carrier transport and lower intrinsic free carrier density of the material. The THz-TDS measurement of $Mo_2Ti_2C_3T_z$ show a similar Drude–Smith low-field conductivity to that of $Ti_3C_2T_x$ (Fig. 13), albeit with a smaller magnitude. In contrast, the OPTP photoconductivity measurement

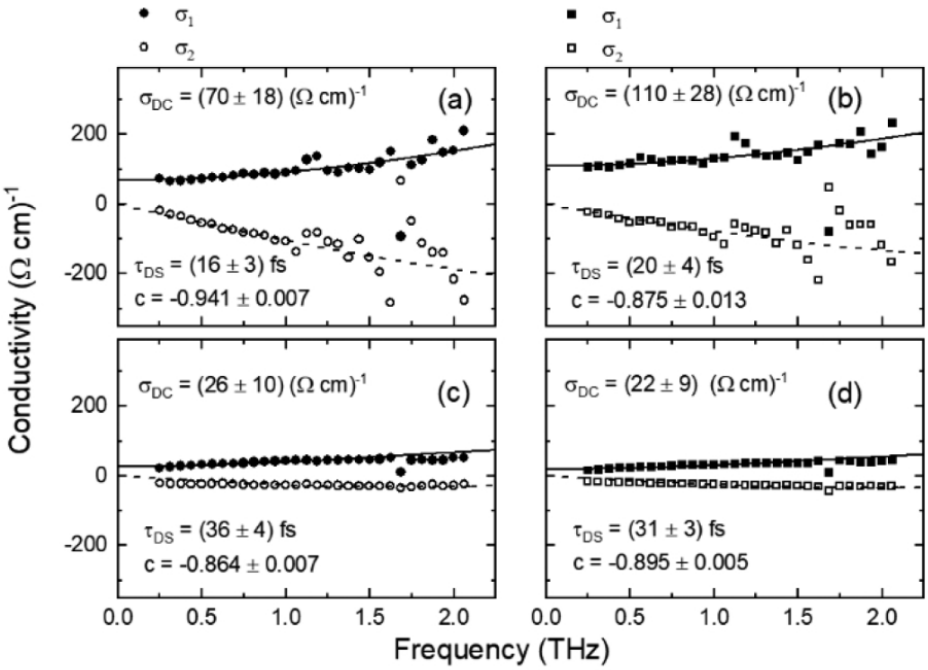

Figure 13. THz-TDS measurement of the sheet conductivity of $Mo_2Ti_2C_3T_z$, (a) without annealing and (b) after 200°C vacuum annealing. (c) $Mo_2TiC_2T_z$ without annealing and (d) $Mo_2TiC_2T_z$ after 200°C vacuum annealing. Conductivity is lower than that of $Ti_3C_2T_z$. Reprinted with permission from [145]. Copyright 2020, American Chemical Society.

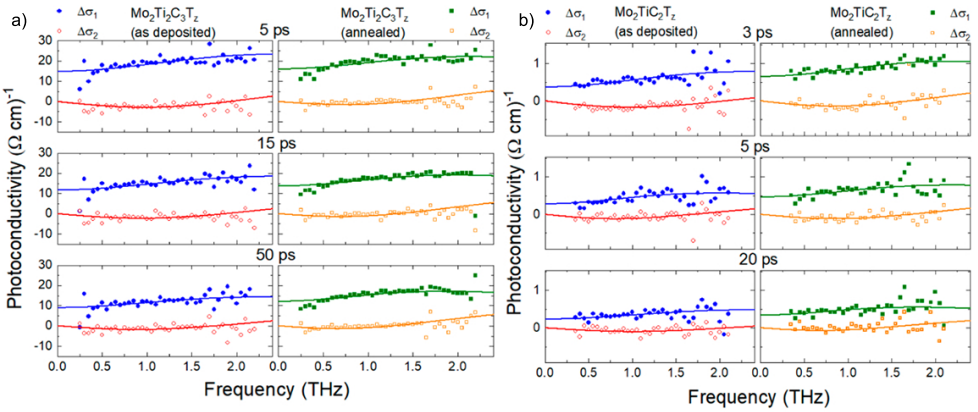

Figure 14. OPTP measurement of the photoconductivity of (a) $Mo_2Ti_2C_3T_z$ at different times after excitation for unannealed sample (left) and annealed at 200°C sample (right). (b) The same quantities as in (a), but for $Mo_2TiC_2T_z$. In contrast to $Ti_3C_2T_x$, MXenes containing Mo exhibit positive photoconductivity, potentially because of carriers moving to the low-effective-mass bands after excitation. Reprinted with permission from [145]. Copyright 2020, American Chemical Society.

(Fig. 13) shows a positive $\Delta\sigma$, possibly because of the higher mobility of photoexcited carriers over the intrinsic carriers that reside in the heavy-average-effective-mass band [145]. Annealing further enhances the transport of photoexcited carriers by reducing the number of carriers trapped around point defects within the nanosheets, nanosheet edges, and at the surface. The behavior of THz photoresponse of Mo-containing MXenes over bare MXenes requites further research is necessary to comprehensively understand electronic transport and defect interaction in MXenes.

5.4. 2D perovskites

2D metal halide perovskites, with lead (Pb) being the most common metal, represent a variation of 3D perovskites. They consist of layers separated by organic molecules and are attractive for potential applications in solar cells due to their high solar-to-electrical energy conversion efficiency, reaching up to 21%, and increased environmental stability compared to their 3D counterparts [234]. These perovskites exhibit a significant exciton population with binding energies ranging between 200 and 300 meV [235]. The carriers in these materials have a polaronic nature, essentially representing free carriers coupled with lattice vibrations [236], making them unique candidates for various optoelectronic applications.

Ruddlesden–Popper (RP) perovskites are the most commonly used 2D perovskites, having the general formula $A_{n+1}B_nX_{3n+1}$, where A and B represent cations, and X denotes an anion, such as oxygen. The variable n in the formula indicates the count of octahedral layers that make up the perovskite-like structure in these materials.

The first OPTP study revealed that reduced screening in 2D perovskites contributes to a lower density of traps and a larger exciton population when moving from bulk to 2D [237]. The presence of excitons in 2D perovskites is further substantiated in recent studies by Burgos-Caminal *et al.* [91]. In this study, ultrabroadband (3-16 THz) time-resolved terahertz spectroscopy (TRTS) (similar to OPTP) and fluorescence upconversion spectroscopies (FLUPS) were employed to probe the formation of excitons. The PEA_2PbI_4 sample was excited at 400 nm and 510 nm, corresponding to the bandgap and excitonic resonance peaks, respectively. Exciting above the band-edge leads to rapid cooling of the carriers and subsequent exciton formation. The photoconductivity spectra follow a non-Drude-type response. The Drude–Smith–Lorentz model is used to incorporate free carrier backscattering and resonance peaks, accounting for inter-excitonic transitions. The presence of long-duration excitons at high densities eliminates the possibility of traditional Mott decomposition into unbound carriers and emphasizes the possibility of biexcitonic interaction and Auger heating.

Similar findings were reported by Folpini *et al.* about the presence of free carriers and excitons in a similar 2D perovskite NBT_2PbI_4 at the THz range [238]. It reported the interaction between polaronic-free carriers and excitons as a major contribution in THz response. A small number of unpaired polarons interact with a large excitonic bath and produce restoring force to localize polarons. Figure 15shows the transient THz conductivity for different pump fluence and probe delays. The photoconductivity follows the Drude-Lorentz model with a free carrier polaronic term and a Lorentzian excitonic resonance term. It is evident that inter-excitonic and exciton-polaron interaction play an important role in THz 2D perovskite transport which requires detailed investigation.

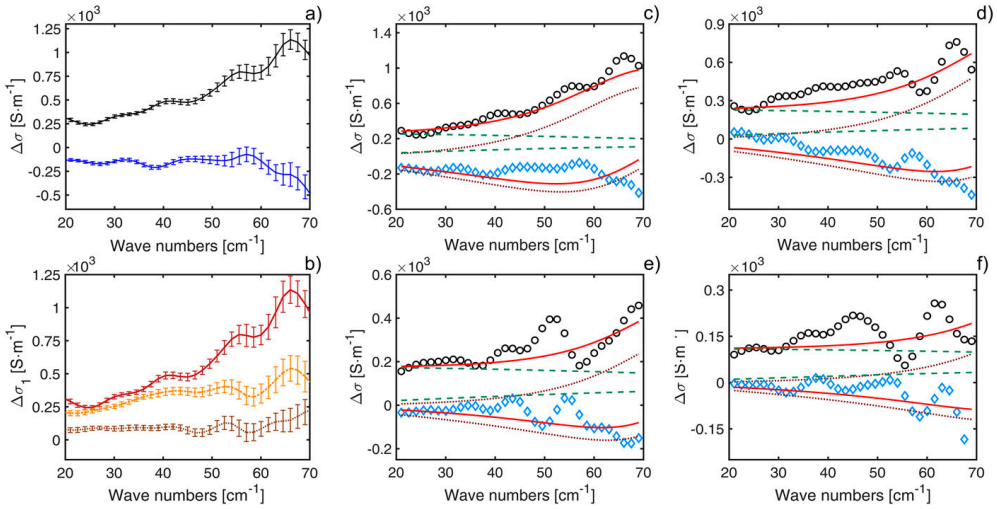

Figure 15. OPTP measurement of the photoinduced complex optical conductivity of the 2D NBT_2PbI_4 perovskite thin film at different pump–probe delays for excitation at 790 nm. (a) Real $\Delta\sigma_1$ (black line) and imaginary $\Delta\sigma_2$ (blue line) parts of the optical conductivity with 65 μJ/cm^{-2} fluence 0.5 ps after the photoexcitation; (b) $\Delta\sigma_1$ acquired 0.5 ps after the photoexcitation at 28 (maroon dotted curve), 50 (yellow dash-dotted curve), and 65 μJ/cm^{-2} fluence (red solid curve); (c)–(f) $\Delta\sigma_1$ (black open circles) and$\Delta\sigma_2$ (blue open diamonds) acquired at 65 μJ/cm^{-2} for 0.5 ps, 1 ps, 2 ps, and 4 ps pump-probe delays, respectively, together with the related Drude–Lorenz fit (red solid curve). The green dashed curve and maroon dotted curve are the Drude and Lorentz contributions to the fit, respectively. The main contributor to the photoconductivity are the charged polaronic carriers interacting with a large excitonic bath. Reprinted with permission from [238], CC–BY 4.0.

5.5. Topological 2D materials

Recent investigations into finding alternatives to traditional 2D materials have led to the discovery of 2D materials with exotic properties.

Topological insulators (TIs) are a new class of quantum material that exhibits insulating bulk states while having gapless surface conducting states that are intrinsically topologically protected by the band structure [239]. The possibility of exciting electrons from the bulk state to the surface state and vice versa in these materials provides an excellent opportunity to use them in optical switching [240, 241] and quantum computing [242]. Bi_2Se_3 and Bi_2Te_3 stand out as frequently explored TI materials because of their 2D nature (metallic surface states independent of thickness) and topological properties.

Photoexcited carrier dynamics of Bi_2Se_3 probed via OPTP with a 2 ps probe delay showed the interplay between topological surface states and bulk states [243]. For Bi_2Se_3 thicknesses less than 15 quintuple layers (QLs), the photoconductivity was negative, transitioning to positive for higher thickness samples at low temperatures (10 K). Similar to graphene, the phenomenon was explained by looking at the ratio of $\Delta D_{\mathrm{Drude}}/\Delta\Gamma_{\mathrm{Drude}}$, which determines the sign of photoconductivity. The TI surface states, which are thickness-independent, contributed to the scattering rate, making the $\Delta D_{\mathrm{Drude}}/\Delta\Gamma_{\mathrm{Drude}}$ ratio small, while for higher thickness samples, bulk

conduction channels opened up, making the ratio large and thus showing positive photoconductance. At higher temperatures (230 K), bulk-phonon-mediated scattering drove bulk electrons to surface states. The additional electrons screen the charged impurities to produce a lower scattering rate, showing positive photoconductivity. Similar results were also reported in another study [83], showing short-lived (∼10 ps) scattering from surface states in thin samples and faster (∼5 ps) rise and decay times coming from bulk contribution in thicker samples. The same group in Ref. [243] reported THz-TDS measurements on 32 QL Bi_2Se_3, with surface electrons dominating the equilibrium conductivity and bulk phonon modes showing up around 2 THz. The bulk Bi_2Se_3 reported the mode at 1 THz [244]. To summarize, the topological surface states in TIs, which can also suppress bulk dissipation, may open up a new frontier in high-performance optoelectronic devices.

5.6. Topological semimetals (TSMs)

Topological semimetals (TSMs), also known as Weyl semimetals, have attracted interest due to their inversion or time-reversal symmetry breaking. They exhibit high nonlinear optical properties [245] and massless Weyl fermions with very high electrical properties [246]. 2D TSMs such as $PdTe_2$, $PtTe_2$, WTe_2, and Mn_3Sn carry topological properties with the added advantage of being 2D in nature. However, studies in the THz range are limited. A recent study showed that 2D TSMs produce record values of THz photoresponse and highly anisotropic THz conductivity [247], owing to the photogalvanic effect caused by topological electrons, making them suitable for THz detection. A polarization-resolved THz-TDS study of thin films of antiferromagnetic Mn_3Sn revealed a longitudinal conductivity as high as 3800 $\Omega^{-1}\text{cm}^{-1}$ and a large anomalous Hall conductivity of 20 $\Omega^{-1}\text{cm}^{-1}$, which is beneficial for spintronic applications [248]. Research in the terahertz application of topological materials is just getting started, showing promising results to date.

5.7. 2D heterostructures

We conclude this section with a brief progress report on vdW Graphene and TMD-based heterostructures, which are promising for THz application as they are not limited by traditional lattice-matching growth conditions and atomic-interdiffusion constraints. Graphene/TMD heterostructures are particularly interesting for harvesting high mobility and conductivity of graphene, as well as high optical absorption of TMDs. OPTP and TA experiment on graphene/MoS_2 heterostructure revealed interlayer exciton with long formation time around 18 ps [249]. The transition from positive to negative photoconductivity in $PtSe_2$/graphene heterostructures modulated by stacking order has been reported [250].

Heterostructures based solely on TMDs generally possess type-II band alignment that facilitates the formation of interlayer excitons [251]. Vertical CVD grown $MoSe_2/MoS_2$ heterostructures exhibit significant enhancements in the THz photoconductivity over single-material structures [252]. CVD-grown $MoTe_2/WTe_2$ heterostructures showed sub-picosecond exciton lifetime, potentially promising for ultrafast THz detectors [253]. Research in graphene and TMD heterostructures is a relatively new field, with many opportunities for development.

6. Conclusion

In this article, we presented a focused review of time-resolved ultrafast THz techniques and their implementation in conductivity and photoconductivity studies of 2D van der Waals materials, along with an overview of materials synthesis and processing and the theoretical models used for the interpretation of conductivity spectra. The studies reveal interesting phenomena, such as negative photoconductivity due to increased scattering rate in graphene at bandgap excitation, the formation of heavy trions in TMD MoS_2, the reduction of mobility in MXenes because of increased boundary scattering, and polaronic interaction in thin-film perovskites at room temperature. The process of neutral and charged bound-exciton formation in 2D semiconductors, leading to either negative or positive photoconductivity needs further exploration. Additionally, strain, magnetic fields, and quantum confinement can also exert significant influence in controlling THz conductivity. For example, introducing in-plane strain can induce a topological phase transition producing spin-controlled current switching in TMDs [254], edge-state currents in bilayer graphene, and magnetic-field-controlled phase shift of polarization dependence [255], as well as an enhancement of charge localization and thus photoconductivity reduction in twisted graphene-MoS_2 heterostructures [256]. There are a number of THz-TDS and OPTP studies on graphene and TMDs, but there is a need for further exploration of other promising 2D materials and structures, such as topological insulators, Weyl semimetals, 2D metamaterials, and their heterostructures.

On the modeling front, while the experimental results are usually fitted with phenomenological models, there is inherent ambiguity in model selection, given that distinct models with different parameters can seemingly fit the data. Thus ultrafast carrier dynamics in emerging 2D materials with a detailed microscopic modeling of charge transport is necessary. Incorporating many-body effects is particularly important in 2D materials, given the high exciton binding energy and increased Coulomb interaction present in 2D materials.

THz spectroscopies are powerful tools for understanding ultrafast carrier dynamics and transport with sub-picosecond resolution. This capability allows us to measure the fundamental physical properties such as density, mobility, and scattering time of carriers, as well as understand the morphology and quality of grown samples by looking at the conductivity spectra. 2D materials appear to have significant potential for next-generation electronic and optoelectronic devices. However, challenges such as environmental stability, which materials like black phosphorus lack, and the need for large-scale synthesis beyond millimeter scale need to be addressed first, although significant progress has been made in automating the synthesis process of 2D materials [257].

However, certain aspects of THz spectroscopy can be further improved. At present, THz imaging resolution is limited by the beam focus size, which depends on the long THz wavelength. This prevents imaging of samples below a few microns in size [17]. One way of solving the issue can be incorporating atomic force microscopy (AFM), which has a finer resolution, with terahertz spectrometers [258, 259]. The sharp conducting tip of AFM can focus the THz beam subwavelength and characterize conductive properties of the sample directly below it. In addition, liquid water has high absorption at THz frequencies, which means THz setups are only useful in controlled laboratory conditions. To compensate for water effects, numerical algorithms can be developed [260, 261]. If the liquid effect is eliminated numerically, more complex

setups can be developed to provide high numerical aperture for improved focusing.

At present, THz spectroscopy techniques are developing fast, incorporating a broad range of probe frequencies and highly tunable pump excitations. These developments are spurred in part by the growing interest in the applications of 2D materials as photonic elements, radiation and shielding devices, and storage systems. We believe this review might serve as a useful resource for upcoming research endeavors into the exciting THz physics of 2D materials.

Acknowledgement

The authors gratefully acknowledge support by the National Science Foundation, Award 2212011 (SM), and by the U.S. Department of Energy Office of Science, Award DE-SC0023178 (LA). Additional support during the writing of this manuscript was provided by the Splinter Professorship and the Vilas Distinguished Achievement Professorship (IK). The original data published in this manuscript were generated using the computing resources and assistance of the UW-Madison Center for High Throughput Computing (CHTC) in the Department of Computer Sciences.

Data Availability Statement

The data that support the findings of this study are available upon reasonable request from the authors.

[1] K. S. Novoselov, A. K. Geim, S. V. Morozov, D. Jiang, Y. Zhang, S. V. Dubonos, I. V. Grigorieva, and A. A. Firsov, "Electric field effect in atomically thin carbon films," *Science*, vol. 306, p. 666–669, Oct. 2004.

[2] A. K. Geim and I. V. Grigorieva, "Van der waals heterostructures," *Nature*, vol. 499, p. 419–425, July 2013.

[3] N. Mounet, M. Gibertini, P. Schwaller, D. Campi, A. Merkys, A. Marrazzo, T. Sohier, I. E. Castelli, A. Cepellotti, G. Pizzi, and N. Marzari, "Two-dimensional materials from high-throughput computational exfoliation of experimentally known compounds," *Nature Nanotechnology*, vol. 13, pp. 246–252, Feb. 2018.

[4] Z. Ni, Q. Liu, K. Tang, J. Zheng, J. Zhou, R. Qin, Z. Gao, D. Yu, and J. Lu, "Tunable bandgap in silicene and germanene," *Nano Letters*, vol. 12, p. 113–118, Dec. 2011.

[5] Z. Li, Y. Liu, A. Zhang, Q. Liu, C. Shen, F. Wu, C. Xu, M. Chen, H. Fu, and C. Zhou, "Quasi-two-dimensional $\beta - Ga_2O_3$ field effect transistors with large drain current density and low contact resistance via controlled formation of interfacial oxygen vacancies," *Nano Research*, vol. 12, p. 143–148, Sept. 2018.

[6] D. Lembke, S. Bertolazzi, and A. Kis, "Single-layer MoS_2 electronics," *Accounts of Chemical Research*, vol. 48, p. 100–110, Jan. 2015.

[7] Z. Yin, H. Li, H. Li, L. Jiang, Y. Shi, Y. Sun, G. Lu, Q. Zhang, X. Chen, and H. Zhang, "Single-layer MoS_2 phototransistors," *ACS Nano*, vol. 6, p. 74–80, Dec. 2011.

[8] W. Choi, M. Y. Cho, A. Konar, J. H. Lee, G. Cha, S. C. Hong, S. Kim, J. Kim, D. Jena, J. Joo, and S. Kim, "High-detectivity multilayer MoS_2 phototransistors with spectral response from ultraviolet to infrared," *Advanced Materials*, vol. 24, p. 5832–5836, Aug. 2012.

[9] O. Lopez-Sanchez, D. Lembke, M. Kayci, A. Radenovic, and A. Kis, "Ultrasensitive photodetectors based on monolayer MoS_2," *Nature Nanotechnology*, vol. 8, p. 497–501, June 2013.

[10] C. Wang, F. Yang, and Y. Gao, "The highly-efficient light-emitting diodes based on transition metal dichalcogenides: from architecture to performance," *Nanoscale Advances*, vol. 2, no. 10, p. 4323–4340, 2020.

[11] M.-L. Tsai, S.-H. Su, J.-K. Chang, D.-S. Tsai, C.-H. Chen, C.-I. Wu, L.-J. Li, L.-J. Chen, and J.-H. He, "Monolayer MoS_2 heterojunction solar cells," *ACS Nano*, vol. 8, p. 8317–8322, July 2014.

[12] P. Han, X. Wang, and Y. Zhang, "Time-resolved terahertz spectroscopy studies on 2D van der waals materials," *Advanced Optical Materials*, vol. 8, Aug. 2019.

[13] M. M. Ugeda, A. J. Bradley, S.-F. Shi, F. H. da Jornada, Y. Zhang, D. Y. Qiu, W. Ruan, S.-K. Mo, Z. Hussain, Z.-X. Shen, F. Wang, S. G. Louie, and M. F. Crommie, "Giant bandgap renormalization and excitonic effects in a monolayer transition metal dichalcogenide semiconductor," *Nature Materials*, vol. 13, p. 1091–1095, Aug. 2014.

[14] W. Lee, L.-S. Lu, W.-H. Chang, and C.-K. Shih, "Momentum-resolved electronic structures of a monolayer-MoS_2/multilayer-$MoSe_2$ heterostructure," *The Journal of Physical Chemistry C*, vol. 125, p. 16591–16597, July 2021.

[15] A. Hanbicki, M. Currie, G. Kioseoglou, A. Friedman, and B. Jonker, "Measurement of high exciton binding energy in the monolayer transition-metal dichalcogenides WS_2 and WSe_2," *Solid State Communications*, vol. 203, p. 16–20, Feb. 2015.

[16] Z. Nie, R. Long, J. S. Teguh, C.-C. Huang, D. W. Hewak, E. K. L. Yeow, Z. Shen, O. V. Prezhdo, and Z.-H. Loh, "Ultrafast electron and hole relaxation pathways in few-layer MoS_2," *The Journal of Physical Chemistry C*, vol. 119, p. 20698–20708, Aug. 2015.

[17] M. Koch, D. M. Mittleman, J. Ornik, and E. Castro-Camus, "Terahertz time-domain spectroscopy," *Nature Reviews Methods Primers*, vol. 3, no. 1, p. 48, 2023.

[18] T. Elsaesser, K. Reimann, and M. Woerner, *Concepts and applications of nonlinear terahertz spectroscopy*. IOP Concise Physics, San Rafael, CA: Morgan & Claypool, Feb. 2019.

[19] S. D. et al., "The 2017 terahertz science and technology roadmap," *J. Phys. D: Appl. Phys.*, vol. 50, p. 043001, 2017.

[20] D. M. Mittleman, "Twenty years of terahertz imaging [invited]," *Optics Express*, vol. 26, p. 9417, Apr. 2018.

[21] C. Jansen, S. Wietzke, O. Peters, M. Scheller, N. Vieweg, M. Salhi, N. Krumbholz, C. Jördens, T. Hochrein, and M. Koch, "Terahertz imaging: applications and perspectives," *Appl. Opt.*, vol. 49, pp. E48–57, July 2010.

[22] L. Yang, T. Guo, X. Zhang, S. Cao, and X. Ding, "Toxic chemical compound detection by terahertz spectroscopy: a review," *Rev. Anal. Chem.*, vol. 37, Sept. 2018.

[23] S. Koenig, D. Lopez-Diaz, J. Antes, F. Boes, R. Henneberger, A. Leuther, A. Tessmann, R. Schmogrow, D. Hillerkuss, R. Palmer, T. Zwick, C. Koos, W. Freude, O. Ambacher,

J. Leuthold, and I. Kallfass, "Wireless sub-THz communication system with high data rate," *Nat. Photonics*, vol. 7, pp. 977–981, Dec. 2013.

[24] M. van Exter and D. R. Grischkowsky, "Characterization of an optoelectronic terahertz beam system," *IEEE Trans. Microw. Theory Tech.*, vol. 38, no. 11, pp. 1684–1691, 1990.

[25] I. F. Akyildiz, J. M. Jornet, and C. Han, "Terahertz band: Next frontier for wireless communications," *Phys. Commun.*, vol. 12, pp. 16–32, Sept. 2014.

[26] H.-J. Song and T. Nagatsuma, "Present and future of terahertz communications," *IEEE Trans. Terahertz Sci. Technol.*, vol. 1, pp. 256–263, Sept. 2011.

[27] F. Bernardo, J. A. Covas, and S. V. Canevarolo, "On-line optical monitoring of the mixing performance in co-rotating twin-screw extruders," *Polymers (Basel)*, vol. 14, p. 1152, Mar. 2022.

[28] F. Rutz, M. Koch, S. Khare, M. Moneke, H. Richter, and U. Ewert, "Terahertz quality control of polymeric products," *Int. J. Infrared Millimeter Waves*, vol. 27, pp. 547–556, Apr. 2006.

[29] P. F. Taday, "Applications of terahertz spectroscopy to pharmaceutical sciences," *Philos. Trans. A Math. Phys. Eng. Sci.*, vol. 362, pp. 351–63; discussion 363–4, Feb. 2004.

[30] W. Jiang, Q. Zhou, J. He, M. A. Habibi, S. Melnyk, M. El-Absi, B. Han, M. D. Renzo, H. D. Schotten, F.-L. Luo, T. S. El-Bawab, M. Juntti, M. Debbah, and V. C. M. Leung, "Terahertz communications and sensing for 6g and beyond: A comprehensive review," *IEEE Communications Surveys & Tutorials*, p. 1–1, 2024.

[31] A. Shafie, N. Yang, C. Han, J. M. Jornet, M. Juntti, and T. Kürner, "Terahertz communications for 6g and beyond wireless networks: Challenges, key advancements, and opportunities," *IEEE Network*, vol. 37, p. 162–169, May 2023.

[32] X. Cai, X. Cheng, and F. Tufvesson, "Toward 6G with terahertz communications: Understanding the propagation channels," *IEEE Commun. Mag.*, vol. 62, pp. 32–38, Feb. 2024.

[33] Y. Zhang and M. S. Shur, "Ultrashort pulse detection and response time analysis using plasma-wave terahertz field-effect transistors," *IEEE Trans. Electron Devices*, vol. 68, pp. 903–910, Feb. 2021.

[34] Y. Zhang and M. S. Shur, "TeraFET terahertz detectors with spatially non-uniform gate capacitances," *Appl. Phys. Lett.*, vol. 119, p. 161104, Oct. 2021.

[35] N. Akter, M. R. Siddiquee, M. Shur, and N. Pala, "AI-powered terahertz VLSI testing technology for ensuring hardware security and reliability," *IEEE Access*, vol. 9, pp. 64499–64509, 2021.

[36] M. Shur, S. Rudin, G. Rupper, M. Reed, and J. Suarez, "Sub-terahertz testing of millimeter wave monolithic and very large scale integrated circuits," *Solid State Electron.*, vol. 155, pp. 44–48, May 2019.

[37] J. B. Baxter and C. A. Schmuttenmaer, "Conductivity of ZnO nanowires, nanoparticles, and thin films using time-resolved terahertz spectroscopy," *J. Phys. Chem. B*, vol. 110, pp. 25229–25239, Dec. 2006.

[38] M. C. Beard, G. M. Turner, and C. A. Schmuttenmaer, "Size-dependent photoconductivity in CdSe nanoparticles as measured by time-resolved terahertz spectroscopy," *Nano Lett.*, vol. 2, pp. 983–987, Sept. 2002.

[39] P. Wu, "Mobility overestimation in molybdenum disulfide transistors due to invasive voltage probes," *Nat. Electron.*, vol. 6, pp. 836–838, Nov. 2023.

[40] H. J. Joyce, C. J. Docherty, Q. Gao, H. H. Tan, C. Jagadish, J. Lloyd-Hughes, L. M. Herz, and M. B. Johnston, "Electronic properties of GaAs, InAs and InP nanowires studied by terahertz spectroscopy," *Nanotechnology*, vol. 24, p. 214006, May 2013.

[41] L. Luo, I. Chatzakis, A. Patz, and J. Wang, "Ultrafast terahertz probes of interacting dark excitons in chirality-specific semiconducting single-walled carbon nanotubes," *Phys. Rev. Lett.*, vol. 114, p. 107402, Mar. 2015.

[42] S. Kar, J. Lake, S. Adeyemo, T. Santra, and H. Joyce, "The physics of terahertz negative photoconductivity in low-dimensional materials," *Materials Today Physics*, vol. 23, p. 100631, Mar. 2022.

[43] W. Zheng, Y. Jiang, X. Hu, H. Li, Z. Zeng, X. Wang, and A. Pan, "Light emission properties of 2D transition metal dichalcogenides: Fundamentals and applications," *Adv. Opt. Mater.*, vol. 6, p. 1800420, Nov. 2018.

[44] X. Xing, Z. Zhang, and G. Ma, "Regulating terahertz photoconductivity in two-dimensional materials," *Photonics*, vol. 10, p. 810, July 2023.

[45] X. Xue, M. Jiang, G. Li, X. Lin, G. Ma, and P. Jin, "Photoinduced insulator-metal phase transition and the metallic phase propagation in VO_2 films investigated by time-resolved terahertz spectroscopy," *J. Appl. Phys.*, vol. 114, p. 193506, Nov. 2013.

[46] J. A. Spies, J. Neu, U. T. Tayvah, M. D. Capobianco, B. Pattengale, S. Ostresh, and C. A. Schmuttenmaer, "Terahertz spectroscopy of emerging materials," *The Journal of Physical Chemistry C*, vol. 124, no. 41, pp. 22335–22346, 2020.

[47] Y. Zhang, J. Dai, X. Zhong, D. Zhang, G. Zhong, and J. Li, "Probing ultrafast dynamics of ferroelectrics by time-resolved pump-probe spectroscopy," *Advanced Science*, vol. 8, no. 22, p. 2102488, 2021.

[48] P. Han, X. Wang, and Y. Zhang, "Time-resolved terahertz spectroscopy studies on 2d van der waals materials," *Advanced Optical Materials*, vol. 8, no. 3, p. 1900533, 2020.

[49] H. Liu, S. L. Wong, and D. Chi, "CVD growth of MoS_2-based two-dimensional materials," *Chemical Vapor Deposition*, vol. 21, no. 10-11-12, pp. 241–259, 2015.

[50] Q. H. Wang, K. Kalantar-Zadeh, A. Kis, J. N. Coleman, and M. S. Strano, "Electronics and optoelectronics of two-dimensional transition metal dichalcogenides," *Nature nanotechnology*, vol. 7, no. 11, pp. 699–712, 2012.

[51] S. W. Han, W. S. Yun, W. J. Woo, H. Kim, J. Park, Y. H. Hwang, T. K. Nguyen, C. T. Le, Y. S. Kim, M. Kang, *et al.*, "Interface defect engineering of a large-scale CVD-grown MoS_2 monolayer via residual sodium at the SiO_2/Si substrate," *Advanced Materials Interfaces*, vol. 8, no. 14, p. 2100428, 2021.

[52] Z. Chen, W. Zhang, C.-A. Palma, A. Lodi Rizzini, B. Liu, A. Abbas, N. Richter, L. Martini, X.-Y. Wang, N. Cavani, *et al.*, "Synthesis of graphene nanoribbons by ambient-pressure chemical vapor deposition and device integration," *Journal of the American Chemical Society*, vol. 138, no. 47, pp. 15488–15496, 2016.

[53] R. Zhao, X. Wei, and H. Zhu, "Edge stabilities, properties and growth kinetics of graphene-like two dimensional monolayers composed with group 15 elements," *Physical Chemistry Chemical Physics*, vol. 24, no. 5, pp. 3348–3356, 2022.

[54] F. Chen, Q. Lv, Q. An, T. Zhang, Y. He, and S. Mao, "Direct CVD-growth and optoelectronic characterizations of monolayer ribbon-like MoS_2 flakes," *Materials Today Communications*, p. 107155, 2023.

[55] X. Niu, Y. Yu, J. Yao, M. Li, J. Sha, and Y. Wang, "Preparation of black phosphorus quantum dots and the surface decoration effect on the monolayer MoS_2 photodetectors," *Chemical Physics Letters*, vol. 772, p. 138571, 2021.

[56] M. Tsigkourakos, M. Kainourgiaki, E. Skotadis, K. P. Giannakopoulos, D. Tsoukalas, and Y. S. Raptis, "Capping technique for chemical vapor deposition of large and uniform MoS_2 flakes," *Thin Solid Films*, vol. 733, p. 138808, 2021.

[57] A. Pelella, A. Grillo, F. Urban, F. Giubileo, M. Passacantando, E. Pollmann, S. Sleziona, M. Schleberger, and A. Di Bartolomeo, "Gate-controlled field emission current from MoS_2 nanosheets," *Advanced Electronic Materials*, vol. 7, no. 2, p. 2000838, 2021.

[58] C. Lan, Z. Zhou, Z. Zhou, C. Li, L. Shu, L. Shen, D. Li, R. Dong, S. Yip, and J. C. Ho, "Wafer-scale synthesis of monolayer WS_2 for high-performance flexible photodetectors by enhanced chemical vapor deposition," *Nano Research*, vol. 11, pp. 3371–3384, 2018.

[59] D. S. Schneider, A. Grundmann, A. Bablich, V. Passi, S. Kataria, H. Kalisch, M. Heuken, A. Vescan, D. Neumaier, and M. C. Lemme, "Highly responsive flexible photodetectors based on movpe grown uniform few-layer MoS_2," *Acs Photonics*, vol. 7, no. 6, pp. 1388–1395, 2020.

[60] B. Kalanyan, W. A. Kimes, R. Beams, S. J. Stranick, E. Garratt, I. Kalish, A. V. Davydov, R. K. Kanjolia, and J. E. Maslar, "Rapid wafer-scale growth of polycrystalline 2H-MoS_2 by pulsed metal–organic chemical vapor deposition," *Chemistry of Materials*, vol. 29, p. 6279–6288, July 2017.

[61] S. M. Eichfeld, L. Hossain, Y.-C. Lin, A. F. Piasecki, B. Kupp, A. G. Birdwell, R. A. Burke, N. Lu, X. Peng, J. Li, A. Azcatl, S. McDonnell, R. M. Wallace, M. J. Kim, T. S. Mayer, J. M. Redwing, and J. A. Robinson, "Highly scalable, atomically thin WSe_2 grown via metal–organic chemical vapor deposition," *ACS Nano*, vol. 9, p. 2080–2087, Feb. 2015.

[62] S. Xie, L. Tu, Y. Han, L. Huang, K. Kang, K. U. Lao, P. Poddar, C. Park, D. A. Muller, R. A. DiStasio, and J. Park, "Coherent, atomically thin transition-metal dichalcogenide superlattices with engineered strain," *Science*, vol. 359, p. 1131–1136, Mar. 2018.

[63] K. Momeni, Y. Ji, N. Nayir, N. Sakib, H. Zhu, S. Paul, T. H. Choudhury, S. Neshani, A. C. T. van Duin, J. M. Redwing, and L.-Q. Chen, "A computational framework for guiding the MOCVD-growth of wafer-scale 2D materials," *npj Computational Materials*, vol. 8, Nov. 2022.

[64] H. Yin, X. Zhang, J. Lu, X. Geng, Y. Wan, M. Wu, and P. Yang, "Substrate effects on the CVD growth of MoS_2 and WS_2," *Journal of Materials Science*, vol. 55, p. 990–996, Sept. 2019.

[65] J. Zhou, J. Lin, X. Huang, Y. Zhou, Y. Chen, J. Xia, H. Wang, Y. Xie, H. Yu, J. Lei, D. Wu, F. Liu, Q. Fu, Q. Zeng, C.-H. Hsu, C. Yang, L. Lu, T. Yu, Z. Shen, H. Lin, B. I. Yakobson, Q. Liu, K. Suenaga, G. Liu, and Z. Liu, "A library of atomically thin metal chalcogenides," *Nature*, vol. 556, p. 355–359, Apr. 2018.

[66] G. Ruan, Z. Sun, Z. Peng, and J. M. Tour, "Growth of graphene from food, insects, and waste," *ACS Nano*, vol. 5, p. 7601–7607, Aug. 2011.

[67] L. Ren, Q. Zhang, J. Yao, Z. Sun, R. Kaneko, Z. Yan, S. Nanot, Z. Jin, I. Kawayama, M. Tonouchi, J. M. Tour, and J. Kono, "Terahertz and infrared spectroscopy of gated large-area graphene," *Nano Lett.*, vol. 12, pp. 3711–3715, July 2012.

[68] N. Rouhi, S. Capdevila, D. Jain, K. Zand, Y. Y. Wang, E. Brown, L. Jofre, and P. Burke, "Terahertz graphene optics," *Nano Res.*, vol. 5, pp. 667–678, Oct. 2012.

[69] J. D. Buron, F. Pizzocchero, B. S. Jessen, T. J. Booth, P. F. Nielsen, O. Hansen, M. Hilke, E. Whiteway, P. U. Jepsen, P. Bøggild, and D. H. Petersen, "Electrically continuous graphene from single crystal copper verified by terahertz conductance spectroscopy and micro four-point probe," *Nano Lett.*, vol. 14, pp. 6348–6355, Nov. 2014.

[70] S. Kar, D. R. Mohapatra, and A. K. Sood, "Tunable terahertz photoconductivity of hydrogen functionalized graphene using optical pump-terahertz probe spectroscopy," *Nanoscale*, vol. 10, pp. 14321–14330, Aug. 2018.

[71] C. J. Docherty, P. Parkinson, H. J. Joyce, M.-H. Chiu, C.-H. Chen, M.-Y. Lee, L.-J. Li, L. M. Herz, and M. B. Johnston, "Ultrafast transient terahertz conductivity of monolayer MoS_2 and WS_2 grown by chemical vapor deposition," *ACS Nano*, vol. 8, pp. 11147–11153, Nov. 2014.

[72] P. Yan, H. Chen, J. Yin, Z. Xu, J. Li, Z. Jiang, W. Zhang, J. Wang, I. L. Li, Z. Sun, and S. Ruan, "Large-area tungsten disulfide for ultrafast photonics," *Nanoscale*, vol. 9, no. 5, p. 1871–1877, 2017.

[73] D. Wang, C. Zhou, A. S. Filatov, W. Cho, F. Lagunas, M. Wang, S. Vaikuntanathan, C. Liu, R. F. Klie, and D. V. Talapin, "Direct synthesis and chemical vapor deposition of 2D carbide and nitride mxenes," *Science*, vol. 379, p. 1242–1247, Mar. 2023.

[74] S. S. Magubane, R. Burns, S. Ngqoloda, C. J. Oliphant, P. F. Miceli, and C. J. Arendse, "Sequential chemical vapor deposition of two-dimensional Sn–Pb compound perovskite thin films and its exciton transport," *ACS Applied Electronic Materials*, vol. 5, p. 5352–5361, July 2023.

[75] A. Y. Cho and J. Arthur, "Molecular beam epitaxy," *Progress in solid state chemistry*, vol. 10, pp. 157–191, 1975.

[76] W. Pacuski, M. Grzeszczyk, K. Nogajewski, A. Bogucki, K. Oreszczuk, J. Kucharek, K. E. Połczynska, B. Seredynski, A. Rodek, R. Bozek, *et al.*, "Narrow excitonic lines and large-scale homogeneity of transition-metal dichalcogenide monolayers grown by molecular beam epitaxy on hexagonal boron nitride," *Nano letters*, vol. 20, no. 5, pp. 3058–3066, 2020.

[77] H. Lind, S. Lidin, and U. Häussermann, "Structure and bonding properties $(Bi_2Se_3)_m(Bi_2)_n$ stacks by first-principles density functional theory," *Physical Review B*, vol. 72, Nov. 2005.

[78] X. F. Kou, L. He, F. X. Xiu, M. R. Lang, Z. M. Liao, Y. Wang, A. V. Fedorov, X. X. Yu, J. S. Tang, G. Huang, X. W. Jiang, J. F. Zhu, J. Zou, and K. L. Wang, "Epitaxial growth of high mobility Bi_2Se_3 thin films on CdS," *Applied Physics Letters*, vol. 98, June 2011.

[79] T. Ginley, Y. Wang, and S. Law, "Topological insulator film growth by molecular beam epitaxy: A review," *Crystals*, vol. 6, p. 154, Nov. 2016.

[80] L. He, F. Xiu, Y. Wang, A. V. Fedorov, G. Huang, X. Kou, M. Lang, W. P. Beyermann, J. Zou, and K. L. Wang, "Epitaxial growth of Bi_2Se_3 topological insulator thin films on Si (111)," *Journal of Applied Physics*, vol. 109, May 2011.

[81] N. Bansal, Y. S. Kim, E. Edrey, M. Brahlek, Y. Horibe, K. Iida, M. Tanimura, G.-H. Li, T. Feng, H.-D. Lee, T. Gustafsson, E. Andrei, and S. Oh, "Epitaxial growth of topological insulator Bi_2Se_3 film on Si(111) with atomically sharp interface," *Thin Solid Films*, vol. 520, p. 224–229, Oct. 2011.

[82] S. Borisova, J. Krumrain, M. Luysberg, G. Mussler, and D. Grützmacher, "Mode of growth of ultrathin topological insulator Bi_2Te_3 films on Si (111) substrates," *Crystal Growth & Design*, vol. 12, p. 6098–6103, Nov. 2012.

[83] R. Valdés Aguilar, J. Qi, M. Brahlek, N. Bansal, A. Azad, J. Bowlan, S. Oh, A. J. Taylor, R. P. Prasankumar, and D. A. Yarotski, "Time-resolved terahertz dynamics in thin films of the topological insulator Bi_2Se_3," *Appl. Phys. Lett.*, vol. 106, p. 011901, Jan. 2015.

[84] T. P. Ginley and S. Law, "Growth of Bi_2Se_3 topological insulator films using a selenium cracker source," *Journal of Vacuum Science & Technology B, Nanotechnology and Microelectronics: Materials, Processing, Measurement, and Phenomena*, vol. 34, Feb. 2016.

[85] Y. Jiang, Y. Y. Sun, M. Chen, Y. Wang, Z. Li, C. Song, K. He, L. Wang, X. Chen, Q.-K. Xue, X. Ma, and S. B. Zhang, "Fermi-level tuning of epitaxial Sb_2Te_3 thin films on graphene by regulating intrinsic defects and substrate transfer doping," *Physical Review Letters*, vol. 108, Feb. 2012.

[86] Y. Kim, A. DiVenere, G. K. L. Wong, J. B. Ketterson, S. Cho, and J. R. Meyer, "Structural and thermoelectric transport properties of Sb_2Te_3 thin films grown by molecular beam epitaxy," *Journal of Applied Physics*, vol. 91, p. 715–718, Jan. 2002.

[87] Y.-J. Chien, Z. Zhou, and C. Uher, "Growth and transport properties of $Sb_{2-x}V_xTe_3$ thin films on sapphire substrates," *Journal of Crystal Growth*, vol. 283, p. 309–314, Oct. 2005.

[88] J. Cao, Z. Guo, S. Zhu, Y. Fu, H. Zhang, Q. Wang, and Z. Gu, "Preparation of lead-free two-dimensional-layered $(C_8H_{17}NH_3)_2SnBr_4$ perovskite scintillators and their application in x-ray imaging," *ACS Applied Materials & Interfaces*, vol. 12, p. 19797–19804, Apr. 2020.

[89] Y. Liu, Y. Zhang, Z. Yang, H. Ye, J. Feng, Z. Xu, X. Zhang, R. Munir, J. Liu, P. Zuo, Q. Li, M. Hu, L. Meng, K. Wang, D.-M. Smilgies, G. Zhao, H. Xu, Z. Yang, A. Amassian, J. Li, K. Zhao, and S. Liu, "Multi-inch single-crystalline perovskite membrane for high-detectivity flexible photosensors," *Nature Communications*, vol. 9, Dec. 2018.

[90] J. W. Jung, S. T. Williams, and A. K.-Y. Jen, "Low-temperature processed high-performance flexible perovskite solar cells via rationally optimized solvent washing treatments," *RSC Adv.*, vol. 4, p. 62971–62977, Nov. 2014.

[91] A. Burgos-Caminal, E. Socie, M. E. F. Bouduban, and J.-E. Moser, "Exciton and carrier dynamics in two-dimensional perovskites," *The Journal of Physical Chemistry Letters*, vol. 11, pp. 7692–7701, Aug. 2020.

[92] K. S. Novoselov, D. Jiang, F. Schedin, T. Booth, V. Khotkevich, S. Morozov, and A. K. Geim, "Two-dimensional atomic crystals," *Proceedings of the National Academy of Sciences*, vol. 102, no. 30, pp. 10451–10453, 2005.

[93] H. Zhao, X. Xing, G. Zhang, W. Liu, H. Dong, Z. Lu, T. Li, J. Zhang, Z. Cheng, L. Wang, *et al.*, "Pmma direct exfoliation for rapid and organic free transfer of centimeter-scale cvd graphene," *2D Materials*, vol. 9, no. 1, p. 015036, 2021.

[94] M. A. Islam, P. Serles, B. Kumral, P. G. Demingos, T. Qureshi, A. Meiyazhagan, A. B. Puthirath, M. S. B. Abdullah, S. R. Faysal, P. M. Ajayan, *et al.*, "Exfoliation mechanisms of 2D materials and their applications," *Applied Physics Reviews*, vol. 9, no. 4, 2022.

[95] B. Radisavljevic, A. Radenovic, J. Brivio, V. Giacometti, and A. Kis, "Single-layer MoS_2 transistors," *Nature Nanotechnology*, vol. 6, pp. 147–150, Jan. 2011.

[96] S. Ooi and H. Ahmad, "Thermal release tape assisted mechanical exfoliation of pristine tmd and the performance of the exfoliated tmd saturable absorbers for q-switched laser generation," *Optical Materials*, vol. 128, p. 112363, 2022.

[97] B. Zhuang, S. Li, S. Li, and J. Yin, "Ways to eliminate pmma residues on graphene——superclean graphene," *Carbon*, vol. 173, pp. 609–636, 2021.

[98] R. Jha and P. K. Guha, "An effective liquid-phase exfoliation approach to fabricate tungsten disulfide into ultrathin two-dimensional semiconducting nanosheets," *Journal of materials science*, vol. 52, pp. 7256–7268, 2017.

[99] R. Frindt, "Single crystals of MoS_2 several molecular layers thick," *Journal of Applied Physics*, vol. 37, no. 4, pp. 1928–1929, 1966.

[100] R. T. Victor, J. R. Marroquin, S. H. Safeer, D. A. Dugato, B. S. Archanjo, L. C. Sampaio, F. Garcia, and J. F. Felix, "Automated mechanical exfoliation technique: a spin pumping study in YIG/TMD heterostructures," *Nanoscale Horizons*, 2023.

[101] A. Jawaid, D. Nepal, K. Park, M. Jespersen, A. Qualley, P. Mirau, L. F. Drummy, and R. A. Vaia, "Mechanism for liquid phase exfoliation of MoS_2," *Chemistry of Materials*, vol. 28, no. 1, pp. 337–348, 2016.

[102] Y. Huang, Y.-H. Pan, R. Yang, L.-H. Bao, L. Meng, H.-L. Luo, Y.-Q. Cai, G.-D. Liu, W.-J. Zhao, Z. Zhou, *et al.*, "Universal mechanical exfoliation of large-area 2D crystals," *Nature communications*, vol. 11, no. 1, p. 2453, 2020.

[103] S. Kim, W. Park, D. Kim, J. Kang, J. Lee, H. Y. Jang, S. H. Song, B. Cho, and D. Lee, "Novel exfoliation of high-quality 2H-MoS_2 nanoflakes for solution-processed photodetector," *Nanomaterials*, vol. 10, no. 6, p. 1045, 2020.

[104] A. A. Pirzado, F. Le Normand, T. Romero, S. Paszkiewicz, V. Papaefthimiou, D. Ihiawakrim, and I. Janowska, "Few-layer graphene from mechanical exfoliation of graphite-based materials: Structure-dependent characteristics," *ChemEngineering*, vol. 3, no. 2, p. 37, 2019.

[105] S. Ott, N. Wolff, F. Rashvand, V. J. Rao, J. Zaumseil, and C. Backes, "Impact of the MoS_2 starting material on the dispersion quality and quantity after liquid phase exfoliation," *Chemistry of Materials*, vol. 31, no. 20, pp. 8424–8431, 2019.

[106] H. Jin, B. Baek, D. Kim, F. Wu, J. D. Batteas, J. Cheon, and D. H. Son, "Effects of direct solvent-quantum dot interaction on the optical properties of colloidal monolayer WS_2 quantum dots," *Nano letters*, vol. 17, no. 12, pp. 7471–7477, 2017.

[107] S. Karunakaran, S. Pandit, B. Basu, and M. De, "Simultaneous exfoliation and functionalization of 2H-MoS_2 by thiolated surfactants: applications in enhanced antibacterial activity," *Journal of the American Chemical Society*, vol. 140, no. 39, pp. 12634–12644, 2018.

[108] M. E. Maldonado, A. Das, A. M. Jawaid, A. J. Ritter, R. A. Vaia, D. A. Nagaoka, P. G. Vianna, L. Seixas, C. J. de Matos, A. Baev, *et al.*, "Nonlinear optical interactions and relaxation in 2D layered transition metal dichalcogenides probed by optical and photoacoustic z-scan methods," *ACS Photonics*, vol. 7, no. 12, pp. 3440–3447, 2020.

[109] R. T. Busch, L. Sun, D. Austin, J. Jiang, P. Miesle, M. A. Susner, B. S. Conner, A. Jawaid, S. T. Becks, K. Mahalingam, *et al.*, "Exfoliation procedure-dependent optical properties of solution deposited MoS_2 films," *npj 2D Materials and Applications*, vol. 7, no. 1, p. 12, 2023.

[110] X. Yang, Z. Chen, J. Fang, Q. Yang, W. Zhao, X. Qian, C. Liu, D. Zhou, S. Tao, and X. Liu, "Efficient exfoliation to MoS_2 nanosheets by salt-assisted refluxing and ultrasonication with photocatalytic application," *Materials Letters*, vol. 255, p. 126596, 2019.

[111] A. Ghorai, S. K. Ray, and A. Midya, "Ethylenediamine-assisted high yield exfoliation of mos2 for flexible solid-state supercapacitor application," *ACS Applied Nano Materials*, vol. 2, no. 3, pp. 1170–1177, 2019.

[112] N. Mayilswamy, A. Krishnan, M. Mundhada, H. Deodhar, G. Joshi, and B. Kandasubramanian, "Shock wave-assisted exfoliation of 2D-material-based polymer nanocomposites: a breakthrough in nanotechnology," *Industrial & Engineering Chemistry Research*, vol. 62, no. 17, pp. 6584–6598, 2023.

[113] G. Eda, H. Yamaguchi, D. Voiry, T. Fujita, M. Chen, and M. Chhowalla, "Photoluminescence from chemically exfoliated MoS_2," *Nano letters*, vol. 11, no. 12, pp. 5111–5116, 2011.

[114] K. Burns, B. Bischoff, C. M. Barr, K. Hattar, and A. Aitkaliyeva, "Photo-exfoliation of MoS_2 quantum dots from nanosheets: an in situ transmission electron microscopy study," *Nanotechnology*, vol. 33, no. 8, p. 085601, 2021.

[115] A. Sunitha, P. Hajara, M. Shaji, M. Jayaraj, and K. Saji, "Luminescent MoS_2 quantum dots with reverse saturable absorption prepared by pulsed laser ablation," *Journal of Luminescence*, vol. 203, pp. 313–321, 2018.

[116] W.-C. Lin, M.-K. Chuang, M. L. Keshtov, G. D. Sharma, and F.-C. Chen, "Photoexfoliation of two-dimensional materials through continuous uv irradiation," *Nanotechnology*, vol. 28, no. 12, p. 125604, 2017.

[117] L. Ali, F. Subhan, M. Ayaz, S. S. u. Hassan, C. C. Byeon, J. S. Kim, and S. Bungau, "Exfoliation of MoS_2 quantum dots: Recent progress and challenges," *Nanomaterials*, vol. 12, no. 19, p. 3465, 2022.

[118] H. Ye, Y. Zhang, A. Wei, D. Han, Y. Liu, W. Liu, Y. Yin, and M. Wang, "Intrinsic-strain-induced curling of free-standing two-dimensional janus mosse quantum dots," *Applied Surface Science*, vol. 519, p. 146251, 2020.

[119] B. Li, L. Jiang, X. Li, P. Ran, P. Zuo, A. Wang, L. Qu, Y. Zhao, Z. Cheng, and Y. Lu, "Preparation of monolayer MoS_2 quantum dots using temporally shaped femtosecond laser ablation of bulk MoS_2 targets in water," *Scientific reports*, vol. 7, no. 1, p. 11182, 2017.

[120] J. Sun, Z. Cheng, Q. Huang, H. He, J. S. Francisco, and S. Du, "Universal principle for large-scale production of a high-quality two-dimensional monolayer via positive charge-driven exfoliation," *The Journal of Physical Chemistry Letters*, vol. 13, no. 28, pp. 6597–6603, 2022.

[121] J. Liu, J. Tang, J. Zhao, Y. Zhao, C. Shen, M. Liao, S. Wang, J. Tian, Y. Chu, J. Li, *et al.*, "Hot-pressed two-dimensional amorphous metals and their electronic properties," *Crystals*, vol. 12, no. 5, p. 616, 2022.

[122] A. Rawson and S. C. K, "Recent advances in terahertz time-domain spectroscopy and imaging techniques for automation in agriculture and food sector," *Food Analytical Methods*, pp. 1–29, 2022.

[123] M. Bernier, F. Garet, J.-L. Coutaz, H. Minamide, and A. Sato, "Accurate characterization of resonant samples in the terahertz regime through a technique combining time-domain spectroscopy and kramers–kronig analysis," *IEEE Transactions on Terahertz Science and Technology*, vol. 6, no. 3, pp. 442–450, 2016.

[124] Q. Wang, L. Xie, and Y. Ying, "Overview of imaging methods based on terahertz time-domain spectroscopy," *Applied Spectroscopy Reviews*, vol. 57, no. 3, pp. 249–264, 2022.

[125] R. M. Smith and M. A. Arnold, "Terahertz time-domain spectroscopy of solid samples:

principles, applications, and challenges," *Applied Spectroscopy Reviews*, vol. 46, no. 8, pp. 636–679, 2011.

[126] D. Markl, P. Bawuah, C. Ridgway, S. van den Ban, D. J. Goodwin, J. Ketolainen, P. Gane, K.-E. Peiponen, and J. A. Zeitler, "Fast and non-destructive pore structure analysis using terahertz time-domain spectroscopy," *International Journal of Pharmaceutics*, vol. 537, no. 1-2, pp. 102–110, 2018.

[127] M. C. Nuss and J. Orenstein, "Terahertz time-domain spectroscopy," *Millimeter and submillimeter wave spectroscopy of solids*, pp. 7–50, 2007.

[128] J.-F. Roux, F. Garet, and J.-L. Coutaz, "Principles and applications of thz time domain spectroscopy," *Physics and applications of terahertz radiation*, pp. 203–231, 2014.

[129] B. Globisch, S. Nellen, R. B. Kohlhaas, L. Liebermeister, and M. Schell, "Terahertz time-domain spectroscopy for non-destructive testing," in *Terahertz, RF, Millimeter, and Submillimeter-Wave Technology and Applications XI*, vol. 10531, pp. 90–96, SPIE, 2018.

[130] P. Bawuah and J. A. Zeitler, "Advances in terahertz time-domain spectroscopy of pharmaceutical solids: A review," *TrAC Trends in Analytical Chemistry*, vol. 139, p. 116272, 2021.

[131] J. Lu, H. Liu, and J. Sun, "Negative terahertz photoconductivity in 2D layered materials," *Nanotechnology*, vol. 28, p. 464001, Oct. 2017.

[132] Y.-C. Shen, X.-Y. Yang, and Z.-J. Zhang, "Broadband terahertz time-domain spectroscopy and fast FMCW imaging: Principle and applications," *Chinese Physics B*, vol. 29, no. 7, p. 078705, 2020.

[133] M. Gezimati and G. Singh, "Terahertz imaging and sensing for healthcare: current status and future perspectives," *IEEE Access*, 2023.

[134] M. Gezimati and G. Singh, "Terahertz imaging technology for localization of cancer tumours: a technical review," *Multimedia Tools and Applications*, pp. 1–37, 2023.

[135] J. Lloyd-Hughes and T.-I. Jeon, "A review of the terahertz conductivity of bulk and nano-materials," *Journal of Infrared, Millimeter, and Terahertz Waves*, vol. 33, pp. 871–925, May 2012.

[136] J. Lu and H. Liu, "A critical review on the carrier dynamics in 2D layered materials investigated using thz spectroscopy," *Optics Communications*, vol. 406, p. 24–35, Jan. 2018.

[137] J. K. Gustafson, P. D. Cunningham, K. M. McCreary, B. T. Jonker, and L. M. Hayden, "Ultrafast carrier dynamics of monolayer WS_2 via broad-band time-resolved terahertz spectroscopy," *The Journal of Physical Chemistry C*, vol. 123, pp. 30676–83, Nov 20 2019.

[138] N. Johnson, "Time resolved terahertz spectroscopy of photocarrier dynamics in WSe_2," 2023.

[139] R. Ulbricht, E. Hendry, J. Shan, T. F. Heinz, and M. Bonn, "Carrier dynamics in semiconductors studied with time-resolved terahertz spectroscopy," *Reviews of Modern Physics*, vol. 83, pp. 543–586, June 2011.

[140] H. J. Joyce, J. L. Boland, C. L. Davies, S. A. Baig, and M. B. Johnston, "A review of the electrical properties of semiconductor nanowires: insights gained from terahertz conductivity spectroscopy," *Semiconductor Science and Technology*, vol. 31, p. 103003, Sept. 2016.

[141] W. Zhang, J. Guo, P. Suo, L. Lv, J. Liu, X. Lin, Z. Jin, W. Liu, and G. Ma, "Optically controlled ultrafast terahertz switching in a CdTe nanostructure thin film," *Applied Optics*, vol. 58, p. 8200, Oct. 2019.

[142] P. Kužel, F. Kadlec, and H. Němec, "Propagation of terahertz pulses in photoexcited media: Analytical theory for layered systems," *The Journal of Chemical Physics*, vol. 127, July 2007.

[143] H. Choi, F. Borondics, D. A. Siegel, S. Y. Zhou, M. C. Martin, A. Lanzara, and R. A. Kaindl, "Broadband electromagnetic response and ultrafast dynamics of few-layer epitaxial graphene," *Appl. Phys. Lett.*, vol. 94, Apr. 2009.

[144] M. Fu, X. Wang, J. Ye, S. Feng, W. Sun, P. Han, and Y. Zhang, "Strong negative terahertz photoconductivity in photoexcited graphene," *Optics Communications*, vol. 406, p. 234–238, Jan. 2018.

[145] G. Li, V. Natu, T. Shi, M. W. Barsoum, and L. V. Titova, "Two-dimensional MXenes $Mo_2Ti_2C_3T_z$ and $Mo_2TiC_2T_z$: Microscopic conductivity and dynamics of photoexcited carriers," *ACS Appl. Energy Mater.*, vol. 3, pp. 1530–1539, Feb. 2020.

[146] P. Y. Han, M. Tani, M. Usami, S. Kono, R. Kersting, and X.-C. Zhang, "A direct comparison between terahertz time-domain spectroscopy and far-infrared fourier transform spectroscopy," *Journal of Applied Physics*, vol. 89, p. 2357–2359, Feb. 2001.

[147] P. Jepsen, D. Cooke, and M. Koch, "Terahertz spectroscopy and imaging – modern techniques and applications," *Laser & Photonics Reviews*, vol. 5, p. 124–166, Oct. 2010.

[148] M. Lundstrom, *Fundamentals of Carrier Transport*. Cambridge, UK: Cambridge University

Press, 2 ed., 2000.

[149] S. Mitra, L. Avazpour, and I. Knezevic, "Terahertz conductivity of monolayer MoS_2," *J. Comput. Electron.*, vol. 22, pp. 1319–1326, Oct. 2023.

[150] K. J. Willis, S. C. Hagness, and I. Knezevic, "A generalized drude model for doped silicon at terahertz frequencies derived from microscopic transport simulation," *Applied Physics Letters*, vol. 102, no. 12, p. 122113, 2013.

[151] M. C. Beard, G. M. Turner, and C. A. Schmuttenmaer, "Transient photoconductivity in GaAs as measured by time-resolved terahertz spectroscopy," *Physical Review B*, vol. 62, pp. 15764–15777, Dec. 2000.

[152] N. Sule, K. J. Willis, S. C. Hagness, and I. Knezevic, "Terahertz-frequency electronic transport in graphene," *Physical Review B*, vol. 90, July 2014.

[153] N. Smith, "Classical generalization of the drude formula for the optical conductivity," *Physical Review B*, vol. 64, Sept. 2001.

[154] N. Smith, "Drude theory and the optical properties of liquid mercury," *Physics Letters A*, vol. 26, pp. 126–127, Jan. 1968.

[155] T.-T. Kang, M. Yamamoto, M. Tanaka, A. Hashimoto, A. Yamamoto, R. Sudo, A. Noda, D. W. Liu, and K. Yamamoto, "Terahertz characterization of semiconductor alloy AlInN: negative imaginary conductivity and its meaning," *Opt. Lett.*, vol. 34, pp. 2507–2509, Aug. 2009.

[156] S. Zhang, Z. Jin, X. Liu, W. Zhao, X. Lin, C. Jing, and G. Ma, "Photoinduced terahertz radiation and negative conductivity dynamics in heusler alloy Co_2MnSn film," *Opt. Lett.*, vol. 42, p. 3080, Aug. 2017.

[157] M. D. Capobianco, S. M. Younan, U. Tayvah, B. Pattengale, J. Neu, J. Gu, and G. W. Brudvig, "Terahertz conductivity of semiconducting 2H and metallic 1T phases of molybdenum disulfide," *The Journal of Physical Chemistry Letters*, vol. 13, pp. 8319–8326, Aug. 2022.

[158] L. V. Titova, T. L. Cocker, S. Xu, J.-M. Baribeau, X. Wu, D. J. Lockwood, and F. A. Hegmann, "Ultrafast carrier dynamics and the role of grain boundaries in polycrystalline silicon thin films grown by molecular beam epitaxy," *Semicond. Sci. Technol.*, vol. 31, p. 105017, Oct. 2016.

[159] X. Zou, J. Luo, D. Lee, C. Cheng, D. Springer, S. K. Nair, S. A. Cheong, H. J. Fan, and E. E. M. Chia, "Temperature-dependent terahertz conductivity of tin oxide nanowire films," *J. Phys. D Appl. Phys.*, vol. 45, p. 465101, Nov. 2012.

[160] K. Yoshioka, Y. Minami, K.-I. Shudo, T. D. Dao, T. Nagao, M. Kitajima, J. Takeda, and I. Katayama, "Terahertz-field-induced nonlinear electron delocalization in Au nanostructures," *Nano Lett.*, vol. 15, pp. 1036–1040, Feb. 2015.

[161] T. L. Cocker, D. Baillie, M. Buruma, L. V. Titova, R. D. Sydora, F. Marsiglio, and F. A. Hegmann, "Microscopic origin of the drude-smith model," *Physical Review B*, vol. 96, Nov. 2017.

[162] T. Ostatnický, V. Pushkarev, H. Němec, and P. Kužel, "Quantum theory of terahertz conductivity of semiconductor nanostructures," *Phys. Rev. B.*, vol. 97, Feb. 2018.

[163] T. Ostatnický, "Linear THz conductivity of nanocrystals," *Opt. Express*, vol. 27, pp. 6083–6088, Mar. 2019.

[164] K. J. Willis, S. C. Hagness, and I. Knezevic, "Multiphysics simulation of high-frequency carrier dynamics in conductive materials," *Journal of Applied Physics*, vol. 110, p. 063714, Sept. 2011.

[165] N. Sule, K. J. Willis, S. C. Hagness, and I. Knezevic, "EMC/FDTD/MD simulation of carrier transport and electrodynamics in two-dimensional electron systems," *Journal of Computational Electronics*, vol. 12, pp. 563–571, Sept. 2013.

[166] K. Tomizawa, *Numerical simulation of submicron semiconductor devices*. Electronic Materials & Devices Library, Norwood, MA: Artech House, Dec. 1993.

[167] P. Y. Yu and M. Cardona, *Fundamentals of semiconductors*. Graduate texts in physics, Berlin, Germany: Springer, 4 ed., May 2010.

[168] D. K. Ferry, *Hot Carriers in Semiconductors*. IOP ebooks, London, England: Institute of Physics Publishing, Dec. 2021.

[169] K. J. Willis, S. C. Hagness, and I. Knezevic, "Terahertz conductivity of doped silicon calculated using the ensemble monte carlo/finite-difference time-domain simulation technique," *Applied Physics Letters*, vol. 96, no. 6, p. 062106, 2010.

[170] K. J. Willis, J. S. Ayubi-Moak, S. C. Hagness, and I. Knezevic, "Global modeling of carrier-field dynamics in semiconductors using EMC–FDTD," *Journal of Computational Electronics*, vol. 8, pp. 153–171, June 2009.

[171] N. Sule, S. C. Hagness, and I. Knezevic, "Clustered impurities and carrier transport in supported graphene," *Phys. Rev. B*, vol. 89, p. 165402, Apr 2014.

[172] F. Karimi, A. H. Davoody, and I. Knezevic, "Dielectric function and plasmons in graphene: A self-consistent-field calculation within a markovian master equation formalism," *Phys. Rev. B.*, vol. 93, May 2016.

[173] F. Karimi, S. Soleimanikahnoj, and I. Knezevic, "Tunable plasmon-enhanced second-order optical nonlinearity in transition metal dichalcogenide nanotriangles," *Phys. Rev. B.*, vol. 103, Apr. 2021.

[174] F. Karimi, S. Mitra, S. Soleimanikahnoj, and I. Knezevic, "Plasmon-enhanced optical nonlinearity in graphene nanomeshes," *Phys. Rev. B.*, vol. 108, July 2023.

[175] M. F. C. M. Quintela, J. C. G. Henriques, L. G. M. Tenório, and N. M. R. Peres, "Theoretical methods for excitonic physics in 2D materials," *physica status solidi (b)*, vol. 259, Apr. 2022.

[176] M. T. Quick, S. Ayari, N. Owschimikow, S. Jaziri, and A. W. Achtstein, "Quantum nature of thz conductivity: Excitons, charges, and trions in 2D semiconductor nanoplatelets and implications for thz imaging and solar hydrogen generation," *ACS Applied Nano Materials*, vol. 5, p. 8306–8313, June 2022.

[177] M. T. Quick, S. Ayari, N. Owschimikow, S. Jaziri, and A. W. Achtstein, "THz mobility and polarizability: impact of transformation and dephasing on the spectral response of excitons in a 2D semiconductor," *Physical Chemistry Chemical Physics*, vol. 25, no. 4, p. 3354–3360, 2023.

[178] A. Hichri, I. Ben Amara, S. Ayari, and S. Jaziri, "Exciton center-of-mass localization and dielectric environment effect in monolayer WS_2," *Journal of Applied Physics*, vol. 121, June 2017.

[179] F. Bonaccorso, Z. Sun, T. Hasan, and A. C. Ferrari, "Graphene photonics and optoelectronics," *Nat. Photonics*, vol. 4, pp. 611–622, Sept. 2010.

[180] M. Jablan, H. Buljan, and M. Soljačić, "Plasmonics in graphene at infrared frequencies," *Phys. Rev. B Condens. Matter Mater. Phys.*, vol. 80, Dec. 2009.

[181] F. H. L. Koppens, D. E. Chang, and F. J. García de Abajo, "Graphene plasmonics: a platform for strong light-matter interactions," *Nano Lett.*, vol. 11, pp. 3370–3377, Aug. 2011.

[182] B. Sensale-Rodriguez, R. Yan, M. M. Kelly, T. Fang, K. Tahy, W. S. Hwang, D. Jena, L. Liu, and H. G. Xing, "Broadband graphene terahertz modulators enabled by intraband transitions," *Nat. Commun.*, vol. 3, p. 780, Apr. 2012.

[183] S. A. Mikhailov, "Graphene-based voltage-tunable coherent terahertz emitter," *Physical Review B*, vol. 87, Mar. 2013.

[184] P. Tassin, T. Koschny, and C. M. Soukoulis, "Applied physics. graphene for terahertz applications," *Science*, vol. 341, pp. 620–621, Aug. 2013.

[185] J. M. Dawlaty, S. Shivaraman, J. Strait, P. George, M. Chandrashekhar, F. Rana, M. G. Spencer, D. Veksler, and Y. Chen, "Measurement of the optical absorption spectra of epitaxial graphene from terahertz to visible," *Appl. Phys. Lett.*, vol. 93, p. 131905, Sept. 2008.

[186] J. Horng, C.-F. Chen, B. Geng, C. Girit, Y. Zhang, Z. Hao, H. A. Bechtel, M. Martin, A. Zettl, M. F. Crommie, Y. R. Shen, and F. Wang, "Drude conductivity of dirac fermions in graphene," *Phys. Rev. B Condens. Matter Mater. Phys.*, vol. 83, Apr. 2011.

[187] Z. Q. Li, E. A. Henriksen, Z. Jiang, Z. Hao, M. C. Martin, P. Kim, H. L. Stormer, and D. N. Basov, "Dirac charge dynamics in graphene by infrared spectroscopy," *Nat. Phys.*, vol. 4, pp. 532–535, July 2008.

[188] M. M. Fogler, D. S. Novikov, and B. I. Shklovskii, "Screening of a hypercritical charge in graphene," *Phys. Rev. B Condens. Matter Mater. Phys.*, vol. 76, Dec. 2007.

[189] A. V. Shytov, M. I. Katsnelson, and L. S. Levitov, "Atomic collapse and quasi-rydberg states in graphene," *Phys. Rev. Lett.*, vol. 99, p. 246802, Dec. 2007.

[190] S. Yuan, R. Roldán, H. De Raedt, and M. I. Katsnelson, "Optical conductivity of disordered graphene beyond the dirac cone approximation," *Phys. Rev. B Condens. Matter Mater. Phys.*, vol. 84, Nov. 2011.

[191] S. H. Abedinpour, G. Vignale, A. Principi, M. Polini, W.-K. Tse, and A. H. MacDonald, "Drude weight, plasmon dispersion, and ac conductivity in doped graphene sheets," *Phys. Rev. B Condens. Matter Mater. Phys.*, vol. 84, July 2011.

[192] L. Ju, B. Geng, J. Horng, C. Girit, M. Martin, Z. Hao, H. A. Bechtel, X. Liang, A. Zettl, Y. R. Shen, and F. Wang, "Graphene plasmonics for tunable terahertz metamaterials," *Nature Nanotechnology*, vol. 6, p. 630–634, Sept. 2011.

[193] J. L. Tomaino, A. D. Jameson, J. W. Kevek, M. J. Paul, A. M. van der Zande, R. A. Barton, P. L. McEuen, E. D. Minot, and Y.-S. Lee, "Terahertz imaging and spectroscopy of large-area single-layer graphene," *Opt. Express*, vol. 19, pp. 141–146, Jan. 2011.

[194] I. Maeng, S. Lim, S. J. Chae, Y. H. Lee, H. Choi, and J.-H. Son, "Gate-controlled nonlinear

conductivity of dirac fermion in graphene field-effect transistors measured by terahertz time-domain spectroscopy," *Nano Lett.*, vol. 12, pp. 551–555, Feb. 2012.

[195] J. D. Buron, F. Pizzocchero, P. U. Jepsen, D. H. Petersen, J. M. Caridad, B. S. Jessen, T. J. Booth, and P. Bøggild, "Graphene mobility mapping," *Sci. Rep.*, vol. 5, p. 12305, July 2015.

[196] V. Pistore, O. Balci, J. Zhang, S. M. Schinde, A. Meersha, A. C. Ferrari, and M. S. Vitiello, "Mapping the complex refractive index of single layer graphene on semiconductor or polymeric substrates at terahertz frequencies," *2d Mater.*, vol. 9, p. 025018, Apr. 2022.

[197] J. D. Buron, D. H. Petersen, P. Bøggild, D. G. Cooke, M. Hilke, J. Sun, E. Whiteway, P. F. Nielsen, O. Hansen, A. Yurgens, and P. U. Jepsen, "Graphene conductance uniformity mapping," *Nano Lett.*, vol. 12, pp. 5074–5081, Oct. 2012.

[198] W. Fuscaldo, S. De Simone, D. Dimitrov, V. Marinova, V. Mussi, R. Beccherelli, and D. C. Zografopoulos, "Terahertz characterization of graphene conductivity via time-domain reflection spectroscopy on metal-backed dielectric substrates," *J. Phys. D Appl. Phys.*, vol. 55, p. 365101, Sept. 2022.

[199] S. A. Jensen, R. Ulbricht, A. Narita, X. Feng, K. Müllen, T. Hertel, D. Turchinovich, and M. Bonn, "Ultrafast photoconductivity of graphene nanoribbons and carbon nanotubes," *Nano Lett.*, vol. 13, pp. 5925–5930, Nov. 2013.

[200] S. Kar, S. Jayanthi, E. Freysz, and A. K. Sood, "Time resolved terahertz spectroscopy of low frequency electronic resonances and optical pump-induced terahertz photoconductivity in reduced graphene oxide membrane," *Carbon N. Y.*, vol. 80, pp. 762–770, Dec. 2014.

[201] P. Kumar, M. Šilhavík, M. R. Parida, H. Němec, J. Červenka, and P. Kužel, "Terahertz charge transport dynamics in 3D graphene networks with localization and band regimes," *Nanoscale Adv.*, vol. 5, pp. 2933–2940, May 2023.

[202] S. Boubanga-Tombet, S. Chan, T. Watanabe, A. Satou, V. Ryzhii, and T. Otsuji, "Ultrafast carrier dynamics and terahertz emission in optically pumped graphene at room temperature," *Phys. Rev. B Condens. Matter Mater. Phys.*, vol. 85, Jan. 2012.

[203] A. Satou, V. Ryzhii, Y. Kurita, and T. Otsuji, "Threshold of terahertz population inversion and negative dynamic conductivity in graphene under pulse photoexcitation," *J. Appl. Phys.*, vol. 113, p. 143108, Apr. 2013.

[204] A. J. Frenzel, C. H. Lui, W. Fang, N. L. Nair, P. K. Herring, P. Jarillo-Herrero, J. Kong, and N. Gedik, "Observation of suppressed terahertz absorption in photoexcited graphene," *Appl. Phys. Lett.*, vol. 102, p. 113111, Mar. 2013.

[205] A. J. Frenzel, C. H. Lui, Y. C. Shin, J. Kong, and N. Gedik, "Semiconducting-to-metallic photoconductivity crossover and temperature-dependent drude weight in graphene," *Phys. Rev. Lett.*, vol. 113, p. 056602, Aug. 2014.

[206] G. Jnawali, Y. Rao, H. Yan, and T. F. Heinz, "Observation of a transient decrease in terahertz conductivity of single-layer graphene induced by ultrafast optical excitation," *Nano Lett.*, vol. 13, pp. 524–530, Feb. 2013.

[207] K. J. Tielrooij, J. C. W. Song, S. A. Jensen, A. Centeno, A. Pesquera, A. Zurutuza Elorza, M. Bonn, L. S. Levitov, and F. H. L. Koppens, "Photoexcitation cascade and multiple hot-carrier generation in graphene," *Nat. Phys.*, vol. 9, pp. 248–252, Apr. 2013.

[208] A. Tomadin, S. M. Hornett, H. I. Wang, E. M. Alexeev, A. Candini, C. Coletti, D. Turchinovich, M. Kläui, M. Bonn, F. H. L. Koppens, E. Hendry, M. Polini, and K.-J. Tielrooij, "The ultrafast dynamics and conductivity of photoexcited graphene at different fermi energies," *Sci. Adv.*, vol. 4, May 2018.

[209] C. J. Docherty, C.-T. Lin, H. J. Joyce, R. J. Nicholas, L. M. Herz, L.-J. Li, and M. B. Johnston, "Extreme sensitivity of graphene photoconductivity to environmental gases," *Nat. Commun.*, vol. 3, no. 1, p. 1228, 2012.

[210] K. F. Mak, K. He, J. Shan, and T. F. Heinz, "Control of valley polarization in monolayer MoS_2 by optical helicity," *Nat. Nanotechnol.*, vol. 7, pp. 494–498, Aug. 2012.

[211] Y. Zhang, T.-R. Chang, B. Zhou, Y.-T. Cui, H. Yan, Z. Liu, F. Schmitt, J. Lee, R. Moore, Y. Chen, H. Lin, H.-T. Jeng, S.-K. Mo, Z. Hussain, A. Bansil, and Z.-X. Shen, "Direct observation of the transition from indirect to direct bandgap in atomically thin epitaxial $MoSe_2$," *Nat. Nanotechnol.*, vol. 9, pp. 111–115, Feb. 2014.

[212] A. O. Slobodeniuk, P. Koutenský, M. Bartoš, F. Trojánek, P. Malý, T. Novotný, and M. Kozák, "Ultrafast valley-selective coherent optical manipulation with excitons in WSe_2 and MoS_2 monolayers," *Npj 2D Mater. Appl.*, vol. 7, pp. 1–7, Mar. 2023.

[213] D. Sun, Y. Rao, G. A. Reider, G. Chen, Y. You, L. Brézin, A. R. Harutyunyan, and T. F. Heinz, "Observation of rapid exciton-exciton annihilation in monolayer molybdenum disulfide," *Nano Lett.*, vol. 14, pp. 5625–5629, Oct. 2014.

[214] Z. Wang, A. Molina-Sánchez, P. Altmann, D. Sangalli, D. De Fazio, G. Soavi, U. Sassi,

F. Bottegoni, F. Ciccacci, M. Finazzi, L. Wirtz, A. C. Ferrari, A. Marini, G. Cerullo, and S. Dal Conte, "Intravalley spin-flip relaxation dynamics in single-layer WS_2," *Nano Lett.*, vol. 18, pp. 6882–6891, Nov. 2018.

[215] J. Lu and H. Liu, "A critical review on the carrier dynamics in 2D layered materials investigated using THz spectroscopy," *Opt. Commun.*, vol. 406, pp. 24–35, Jan. 2018.

[216] T. Kang, T. W. Tang, B. Pan, H. Liu, K. Zhang, and Z. Luo, "Strategies for controlled growth of transition metal dichalcogenides by chemical vapor deposition for integrated electronics," *ACS Mater. Au*, vol. 2, pp. 665–685, Nov. 2022.

[217] C. H. Lui, A. J. Frenzel, D. V. Pilon, Y.-H. Lee, X. Ling, G. M. Akselrod, J. Kong, and N. Gedik, "Trion-induced negative photoconductivity in monolayer MoS_2," *Phys. Rev. Lett.*, vol. 113, p. 166801, Oct. 2014.

[218] P. D. Cunningham, K. M. McCreary, A. T. Hanbicki, M. Currie, B. T. Jonker, and L. M. Hayden, "Charge trapping and exciton dynamics in large-area CVD grown MoS_2," *J. Phys. Chem. C Nanomater. Interfaces*, vol. 120, pp. 5819–5826, Mar. 2016.

[219] S. Kar, Y. Su, R. R. Nair, and A. K. Sood, "Probing photoexcited carriers in a few-layer MoS_2 laminate by time-resolved optical pump-terahertz probe spectroscopy," *ACS Nano*, vol. 9, pp. 12004–12010, Dec. 2015.

[220] J. H. Strait, P. Nene, and F. Rana, "High intrinsic mobility and ultrafast carrier dynamics in multilayer metal-dichalcogenide MoS_2," *Phys. Rev. B Condens. Matter Mater. Phys.*, vol. 90, Dec. 2014.

[221] S. Xu, J. Yang, H. Jiang, F. Su, and Z. Zeng, "Transient photoconductivity and free carrier dynamics in a monolayer WS_2 probed by time resolved terahertz spectroscopy," *Nanotechnology*, vol. 30, p. 265706, June 2019.

[222] J. K. Gustafson, P. D. Cunningham, K. M. McCreary, B. T. Jonker, and L. M. Hayden, "Ultrafast carrier dynamics of monolayer WS_2 via broad-band time-resolved terahertz spectroscopy," *J. Phys. Chem. C Nanomater. Interfaces*, vol. 123, pp. 30676–30683, Dec. 2019.

[223] H. M. Dong, Z. H. Tao, L. L. Li, F. Huang, W. Xu, and F. M. Peeters, "Substrate dependent terahertz response of monolayer WS_2," *Appl. Phys. Lett.*, vol. 116, p. 203108, May 2020.

[224] C. He, L. Zhu, Q. Zhao, Y. Huang, Z. Yao, W. Du, Y. He, S. Zhang, and X. Xu, "Competition between free carriers and excitons mediated by defects observed in layered WSe_2 crystal with time-resolved terahertz spectroscopy," *Adv. Opt. Mater.*, vol. 6, p. 1800290, Oct. 2018.

[225] P. Gopalan, A. Chanana, S. Krishnamoorthy, A. Nahata, M. A. Scarpulla, and B. Sensale-Rodriguez, "Ultrafast THz modulators with WSe_2 thin films [invited]," *Opt. Mater. Express*, vol. 9, p. 826, Feb. 2019.

[226] E. Colin-Ulloa, A. Fitzgerald, K. Montazeri, J. Mann, V. Natu, K. Ngo, J. Uzarski, M. W. Barsoum, and L. V. Titova, "Ultrafast spectroscopy of plasmons and free carriers in 2D MXenes," *Adv. Mater.*, vol. 35, p. e2208659, Feb. 2023.

[227] K. Hantanasirisakul and Y. Gogotsi, "Electronic and optical properties of 2D transition metal carbides and nitrides (MXenes)," *Adv. Mater.*, vol. 30, p. 1804779, Dec. 2018.

[228] T. S. Mathis, K. Maleski, A. Goad, A. Sarycheva, M. Anayee, A. C. Foucher, K. Hantanasirisakul, C. E. Shuck, E. A. Stach, and Y. Gogotsi, "Modified MAX phase synthesis for environmentally stable and highly conductive Ti_2C_3 MXene," *ACS Nano*, vol. 15, pp. 6420–6429, Apr. 2021.

[229] Y. I. Jhon, M. Seo, and Y. M. Jhon, "First-principles study of a MXene terahertz detector," *Nanoscale*, vol. 10, no. 1, pp. 69–75, 2018.

[230] F. Shahzad, M. Alhabeb, C. B. Hatter, B. Anasori, S. Man Hong, C. M. Koo, and Y. Gogotsi, "Electromagnetic interference shielding with 2D transition metal carbides (MXenes)," *Science*, vol. 353, pp. 1137–1140, Sept. 2016.

[231] G. Li, N. Amer, H. A. Hafez, S. Huang, D. Turchinovich, V. N. Mochalin, F. A. Hegmann, and L. V. Titova, "Dynamical control over terahertz electromagnetic interference shielding with 2D $Ti_3C_2T_y$ MXene by ultrafast optical pulses," *Nano Lett.*, vol. 20, pp. 636–643, Jan. 2020.

[232] G. Li, K. Kushnir, Y. Dong, S. Chertopalov, A. M. Rao, V. N. Mochalin, R. Podila, and L. V. Titova, "Equilibrium and non-equilibrium free carrier dynamics in 2D $Ti_3C_2T_x$ MXenes: THz spectroscopy study," *2d Mater.*, vol. 5, p. 035043, June 2018.

[233] E. Li, J. Wei, T. Zhang, H. Wan, Y. Cheng, J. Xie, H. Li, K. Zhang, J. Xu, J. Hu, Q. Wen, X. Xiao, T. Zhao, M. Hu, F. Su, T. Wang, and G. Fang, "Charge carriers localization effect revealed through terahertz spectroscopy of MXene: $Ti_3C_2T_x$," *Small*, Dec. 2023.

[234] M. Shao, T. Bie, L. Yang, Y. Gao, X. Jin, F. He, N. Zheng, Y. Yu, and X. Zhang, "Over 21% efficiency stable 2D perovskite solar cells," *Adv. Mater.*, vol. 34, p. e2107211, Jan. 2022.

[235] E. Cinquanta, E. A. A. Pogna, L. Gatto, S. Stagira, and C. Vozzi, "Charge carrier dynamics in 2D materials probed by ultrafast THzspectroscopy," *Adv. Phys. X.*, vol. 8, Dec. 2023.

[236] F. Thouin, D. A. Valverde-Chávez, C. Quarti, D. Cortecchia, I. Bargigia, D. Beljonne, A. Petrozza, C. Silva, and A. R. Srimath Kandada, "Phonon coherences reveal the polaronic character of excitons in two-dimensional lead halide perovskites," *Nat. Mater.*, vol. 18, pp. 349–356, Apr. 2019.

[237] R. L. Milot, R. J. Sutton, G. E. Eperon, A. A. Haghighirad, J. Martinez Hardigree, L. Miranda, H. J. Snaith, M. B. Johnston, and L. M. Herz, "Charge-carrier dynamics in 2D hybrid metal–halide perovskites," *Nano Lett.*, vol. 16, pp. 7001–7007, Nov. 2016.

[238] G. Folpini, L. Gatto, D. Cortecchia, M. Devetta, G. Crippa, C. Vozzi, S. Stagira, A. Petrozza, and E. Cinquanta, "Ultrafast charge carrier dynamics in quantum confined 2D perovskite," *The Journal of Chemical Physics*, vol. 152, June 2020.

[239] M. Z. Hasan and C. L. Kane, "Colloquium: Topological insulators," *Rev. Mod. Phys.*, vol. 82, pp. 3045–3067, Nov. 2010.

[240] R. Mondal, A. Arai, Y. Saito, P. Fons, A. V. Kolobov, J. Tominaga, and M. Hase, "Coherent dirac plasmons in topological insulators," *Phys. Rev. B.*, vol. 97, Apr. 2018.

[241] H. Luo, *Advanced topological insulators.* Wiley-Scrivener, Apr. 2019.

[242] D. Hsieh, D. Qian, L. Wray, Y. Xia, Y. S. Hor, R. J. Cava, and M. Z. Hasan, "A topological dirac insulator in a quantum spin hall phase," *Nature*, vol. 452, pp. 970–974, Apr. 2008.

[243] S. Sim, M. Brahlek, N. Koirala, S. Cha, S. Oh, and H. Choi, "Ultrafast terahertz dynamics of hot dirac-electron surface scattering in the topological insulator Bi_2Se_3," *Phys. Rev. B Condens. Matter Mater. Phys.*, vol. 89, Apr. 2014.

[244] P. Sharma, M. Kumar, V. P. S. Awana, A. Singh, H. Gohil, and S. S. Prabhu, "Comprehensive analysis of terahertz frequency response of Bi_2Se_3 and Bi_2Te_3 single crystals using terahertz time-domain spectroscopy," *Mater. Sci. Eng. B Solid State Mater. Adv. Technol.*, vol. 272, p. 115355, Oct. 2021.

[245] J. Ma, Q. Gu, Y. Liu, J. Lai, P. Yu, X. Zhuo, Z. Liu, J.-H. Chen, J. Feng, and D. Sun, "Nonlinear photoresponse of type-II weyl semimetals," *Nat. Mater.*, vol. 18, pp. 476–481, May 2019.

[246] N. P. Armitage, E. J. Mele, and A. Vishwanath, "Weyl and dirac semimetals in three-dimensional solids," *Rev. Mod. Phys.*, vol. 90, Jan. 2018.

[247] J. Zhang, T. Zhang, L. Yan, C. Zhu, W. Shen, C. Hu, H. Lei, H. Luo, D. Zhang, F. Liu, Z. Liu, J. Tong, L. Zhou, P. Yu, and G. Yang, "Colossal room-temperature terahertz topological response in type-II weyl semimetal $NbIrTe_4$," *Adv. Mater.*, vol. 34, p. e2204621, Oct. 2022.

[248] T. Matsuda, N. Kanda, T. Higo, N. P. Armitage, S. Nakatsuji, and R. Matsunaga, "Room-temperature terahertz anomalous hall effect in weyl antiferromagnet Mn_3Sn thin films," *Nat. Commun.*, vol. 11, p. 909, Feb. 2020.

[249] Y. Zou, Q.-S. Ma, Z. Zhang, R. Pu, W. Zhang, P. Suo, K. Sun, J. Chen, D. Li, H. Ma, X. Lin, Y. Leng, W. Liu, J. Du, and G. Ma, "Observation of ultrafast interfacial exciton formation and relaxation in graphene/MoS_2 heterostructure," *J. Phys. Chem. Lett.*, pp. 5123–5130, June 2022.

[250] Q.-S. Ma, W. Zhang, C. Wang, R. Pu, C.-W. Ju, X. Lin, Z. Zhang, W. Liu, and R. Li, "Hot carrier transfer in a graphene/$PtSe_2$ heterostructure tuned by a substrate-introduced effective electric field," *J. Phys. Chem. C Nanomater. Interfaces*, vol. 125, pp. 9296–9302, May 2021.

[251] A. Castellanos-Gomez, X. Duan, Z. Fei, H. R. Gutierrez, Y. Huang, X. Huang, J. Quereda, Q. Qian, E. Sutter, and P. Sutter, "Van der waals heterostructures," *Nat. Rev. Methods Primers*, vol. 2, July 2022.

[252] S. Kumar, A. Singh, S. Kumar, A. Nivedan, M. Tondusson, J. Degert, J. Oberlé, S. J. Yun, Y. H. Lee, and E. Freysz, "Enhancement in optically induced ultrafast THz response of $MoSe_2MoS_2$ heterobilayer," *Opt. Express*, vol. 29, p. 4181, Feb. 2021.

[253] K. Lee, J. Li, L. Cheng, J. Wang, D. Kumar, Q. Wang, M. Chen, Y. Wu, G. Eda, E. E. M. Chia, H. Chang, and H. Yang, "Sub-picosecond carrier dynamics induced by efficient charge transfer in $MoTe_2/WTe_2$ van der waals heterostructures," *ACS Nano*, vol. 13, pp. 9587–9594, Aug. 2019.

[254] H. Xu, H. Wang, J. Zhou, Y. Guo, J. Kong, and J. Li, "Colossal switchable photocurrents in topological janus transition metal dichalcogenides," *Npj Comput. Mater.*, vol. 7, Feb. 2021.

[255] S. Candussio, M. V. Durnev, S. A. Tarasenko, J. Yin, J. Keil, Y. Yang, S.-K. Son, A. Mishchenko, H. Plank, V. V. Bel'kov, S. Slizovskiy, V. Fal'ko, and S. D. Ganichev, "Edge photocurrent driven by terahertz electric field in bilayer graphene," *Phys. Rev. B.*, vol. 102, July 2020.

[256] D. Luo, J. Tang, X. Shen, F. Ji, J. Yang, S. Weathersby, M. E. Kozina, Z. Chen, J. Xiao, Y. Ye, T. Cao, G. Zhang, X. Wang, and A. M. Lindenberg, "Twist-angle-dependent ultrafast charge transfer in MoS_2-graphene van der waals heterostructures," *Nano Lett.*, vol. 21, pp. 8051–8057, Oct. 2021.

[257] T. Potočnik, P. J. Christopher, R. Mouthaan, T. Albrow-Owen, O. J. Burton, C. Jagadish, H. H. Tan, T. D. Wilkinson, S. Hofmann, H. J. Joyce, and J. A. Alexander-Webber, "Automated computer vision-enabled manufacturing of nanowire devices," *ACS Nano*, vol. 16, pp. 18009–18017, Nov. 2022.

[258] H. Zhan, V. Astley, M. Hvasta, J. A. Deibel, D. M. Mittleman, and Y.-S. Lim, "The metal-insulator transition in VO_2 studied using terahertz apertureless near-field microscopy," *Applied Physics Letters*, vol. 91, Oct. 2007.

[259] A. J. Huber, F. Keilmann, J. Wittborn, J. Aizpurua, and R. Hillenbrand, "Terahertz near-field nanoscopy of mobile carriers in single semiconductor nanodevices," *Nano Letters*, vol. 8, p. 3766–3770, Oct. 2008.

[260] M. Mikerov, J. Ornik, and M. Koch, "Removing water vapor lines from THz-TDS data using neural networks," *IEEE Transactions on Terahertz Science and Technology*, vol. 10, p. 397–403, July 2020.

[261] W. Withayachumnankul, B. M. Fischer, and D. Abbott, "Numerical removal of water vapour effects from terahertz time-domain spectroscopy measurements," *Proceedings of the Royal Society A: Mathematical, Physical and Engineering Sciences*, vol. 464, p. 2435–2456, May 2008.